



**Politecnico  
di Torino**

**ScuDo**  
Scuola di Dottorato ~ Doctoral School  
WHAT YOU ARE, TAKES YOU FAR

Doctoral Dissertation

Doctoral Program in  
Bioengineering and Medical-Surgical Sciences (33th Cycle)

# **The fracture healing studies: mechanical design and numerical evaluation of a novel wireless dynamizable plate**

**Giancarlo Dichio**

\*\*\*\*\*

**Supervisors**

Prof. Alberto Luigi Audenino

Politecnico di Torino 2021

**Doctoral Examination Committee:**

Prof. Giordano Franceschini, Referee, University of Perugia

Prof. Chiara Giulia Fontanella, Referee, University of Padova

Prof. Piero Pavan, Referee, University of Padova

**Tutors:**

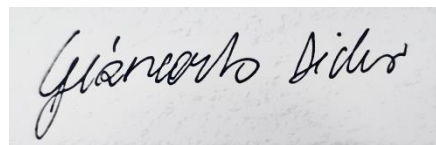
Prof. Alberto Luigi Audenino, Politecnico di Torino

Prof. Alessandro Massé, Politecnico di Torino

Prof. Silvia Spriano, Politecnico di Torino

This thesis is licensed under a Creative Commons License, Attribution – Noncommercial – NoDerivative Works 4.0 International: see [www.creativecommons.org](http://www.creativecommons.org). The text may be reproduced for non-commercial purposes, provided that credit is given to the original author.

I hereby declare that, the contents and organization of this dissertation constitute my own original work and do not compromise in any way the rights of third parties, including those relating to the security of personal data.

A rectangular box containing a handwritten signature in black ink. The signature is written in a cursive style and appears to read "Giancarlo Diller".

.....  
Turin – December 13, 2021



# Academic curriculum vitae

Full name: Giancarlo Dichio

Date of birth: 18/10/1989

Place of birth: Modugno, Bari

Residence: Montescaglioso (MT)

Nationality: Italian

E-mail: [giancarlo.dichio@polito.it](mailto:giancarlo.dichio@polito.it)

## List of publications:

- Dichio, G., Cali, M., Terzini, M., Putame, G., Zanetti, E. M., Costa, P., & Audenino, A. L. (2020). Engineering and Manufacturing of a Dynamizable Fracture Fixation Device System. *Applied Sciences*, 10(19), 6844.
- Dichio, G.; Putame, G.; Terzini, M.; Cannata, S.; Costa, P.; Pasero, E.G.; Audenino, A.L.; Internal fixation of femur fractures: a new wireless electromechanical dynamization system; Pedrizetti, G., Accardo, A., Marceglia, S., Brun, F., Eds.; 2020.
- Terzini, M.; Serino, G.; Lugas, T.A.; Dichio, G.; Costa, P.; Audenino, A.L. Strategies to Speed up the Standardized Bone Plates Mechanical Testing for Regulatory Purposes; Pedrizetti, G., Accardo, A., Marceglia, S., Brun, F., Eds.; 2020;

- G. Putame, G. Pascoletti, G. Franceschini, G. Dichio and M. Terzini, "Prosthetic Hip ROM from Multibody Software Simulation," 2019 41st Annual International Conference of the IEEE Engineering in Medicine and Biology Society (EMBC), Berlin, Germany, 2019, pp. 5386-5389.
- Pascoletti, G., Dichio, G., Marmotti, A., Baroncelli, A. B., Costa, P., Lugas, A. T., & Serino, G. (2019). A novel technique for testing osteointegration.

### **List of conferences:**

- "Internal fixation of femur fractures: a new wireless electromechanical dynamization system." Oral presentation: *GNB 2020, Virtual, 2020*.

# Abstract

The present work illustrates the dynamization of an orthopedic plate for internal fracture fixation, which is thought to shorten healing times and enhance the newly formed bone's quality. The dynamization is performed thanks to a magnetic coupling wirelessly. The thesis shows the peculiarities of the design and manufacturing of this system: it involves two components, sliding concerning each other with an undetermined coefficient of friction and with a specific compounded geometry; there are stringent limits on component size and the required activation energy. Finally, the device belongs to medical devices and, as such, it must comply with the respective regulation (*EU 2017/745, ASTM F382*). The design of the dynamizable fracture fixation plate has required verifying the dynamic of the unlocking mechanism through developing a parametric multi-body model, which has allowed us to fix the main design variables. As a second step, the fatigue strength of the device and the static strength of the whole bone-plate system were evaluated by finite element analysis. Both analyses have contributed to defining the final optimized geometry and the constitutive materials of the plate; finally, the respective working process was set up, and its performance was tested experimentally on a fractured reference femur. The second part of the work is oriented to evaluate the fracture healing properties of the plate in the first post-operative stages. Those results have highlighted the positive behavior of the

Dynamic Plate for what concerns horizontal fractures, compared to a traditional Static Plate. On the whole, the performance of this dynamic plate was proved to be equal or superior to those measured for static plates already on the market, with excellent clinical results. At the same time, pre-clinical tests will be an exciting step of future research, for which more prototypes are now being produced.



# Table of contents

1. Introduction.....	1
1.1 Main clinical problem.....	2
1.2 Aims and objectives.....	2
2. State-of-the-art.....	4
2.1 Fracture healing studies .....	5
2.1.1 Mechanical factors influencing the fracture gap.....	5
2.1.2 Different types of fracture treatments .....	7
2.1.3 Numerical modeling of the secondary fracture healing .....	7
2.2 Dynamization systems .....	9
2.2.1 The mechanotransduction process .....	9
2.2.2 In-vivo monitoring of callus stiffness .....	10
2.2.3 Loading frequency and peak strain magnitude .....	11
3. Conceptual phase .....	13
3.1 Mechanical plate interactions .....	14
3.1.1 Design of the un-locking geometry.....	15
3.1.2 Pin shear section: force evaluation.....	16
3.1.3 Spring action: physical evaluation .....	17
3.2 Electrical parts integration .....	21
3.2.1 Actuation system integration.....	21
3.2.2 Magnetic power supply .....	22
3.3 Setup of the manufacturing flow .....	25
4. Numerical and experimental strategies.....	26
4.1 Multi-body method .....	27
4.1.1 Modeling the un-locking mechanism.....	28

4.2	FE analysis for certification purposes.....	31
4.2.1	Full setup and boundary conditions .....	32
4.2.2	Mesh and material properties .....	33
4.2.3	Internal constraint and interactions .....	34
4.2.4	Contact description and parameters .....	36
4.2.5	Simplified setup description.....	37
4.3	Experimental test setup.....	38
4.4	FE model for fracture healing study .....	40
4.4.1	Building the new FE model.....	41
4.4.2	Selecting the worst physiologic load condition .....	41
5.	Results and discussion .....	43
5.1	Multi-body analysis of the un-locking mechanism.....	44
5.2	FE analysis of the certification tests .....	46
5.2.1	Evaluation of plate fatigue limit.....	46
5.2.2	Evaluation of static structural strength.....	48
5.2.3	Evaluation of the maximum pressure contact .....	50
5.3	Experimental results .....	51
5.4	FE analysis of the fracture healing process .....	53
5.4.1	Main results of the horizontal fracture .....	53
5.4.2	Analysis of different fracture gap .....	58
5.4.3	Analysis of different elastic modulus.....	62
5.4.4	Analysis of minimum and maximum values of IFS.....	66
5.4.5	Plate structural stiffness without callus tissue.....	74
5.4.6	Main limitations of the analysis .....	76
6.	Conclusion .....	77
	References.....	79



# List of abbreviations

FEA – Finite Element Analysis

FE – Finite Element

DOE – Design of Experiment

CAD – Computer-Aided Design

CAE – Computer-Aided Engineering

ASTM – American Society for Testing and Materials

DC – Direct Current

AC – Alternate Current

EU – European Union

IFS – Interfragmentary Strain

IFM – Interfragmentary Movement

MB – Multi-Body analysis

EM – Electro-Mechanical

AO – Association For Osteosynthesis

OTA – Orthopaedic Trauma Association

2D – Bi-Dimensional

3D – Tri-Dimensional

# List of Figures

<b>Figure 1:</b> Conceptual design of the plate dynamization system.....	15
<b>Figure 2:</b> Detail the unlocking mechanism in locked (A) and unlocked (B) configuration. ....	15
<b>Figure 3:</b> Main parameters for the calculation of the spring pre-setting. ....	18
<b>Figure 4:</b> The metal brush motor with the four stages gear reduction system and the preselected screw drive in the assembled configuration. ....	22
<b>Figure 5</b> Left image: detail of the internal actuation system of the plate: A) pin; B) wedge-shaped block; C) brush motor; D) receiver circuit; E) receiver coil. Right image: Detail the locking mechanism in the locked (1) and un-locked (2) configurations. ....	24
<b>Figure 6:</b> Multi-body model of the un-locking mechanism with an overview of its principal components.....	30
<b>Figure 7:</b> Refined plate design: internal components (a) and external parts (b). ....	31
<b>Figure 8:</b> The FE model, according to the overall setup, indicates the respective loads and boundary constraints; one screw section model has been highlighted in the circle below.....	32
<b>Figure 9:</b> Main constraints related to plate internal components (a, b, c) and section detail the mechanical play between the multiple parts (d, e). ....	35
<b>Figure 10:</b> The simplified FE model with constraints and loads applied to this specific plate. ....	37
<b>Figure 11:</b> Four-point bending test with Instron Electropulse E3000: (a) loading set up; (b) plate detail.....	39
<b>Figure 12:</b> Standard of fracture types following the AO/OTA classification.	40
<b>Figure 13:</b> Main results of multi-body model (friction coefficient: 0.15, spring stiffness: 20 N/mm). ....	45
<b>Figure 14:</b> Maximum von Mises stress at fatigue bending limit of 29 N·m; detail pin section (A-A) and plate body shrinkage. ....	47
<b>Figure 15:</b> Haigh diagram at fatigue bending limit of 29 N·m, obtained with $R=0.1$ factor and a stress amplitude limit of 400 MPa.....	47
<b>Figure 16:</b> Maximum von Mises stress [MPa], at peak static load of 2 kN; detail of the entire plate components and the most stressed screws. ....	49
<b>Figure 17:</b> Maximum von Mises stress [MPa], at 33% of experimental peak static load: 660 N; detail of the principal plate components and the most stressed screws (A and B boxes). ....	49

<b>Figure 18:</b> Maximum contact pressure [MPa] at the peak static load of 2 kN with detail of structural plate components.....	50
<b>Figure 19:</b> Force-displacement curves obtained from the experimental tests for integer and fractured samples: the red arrow marks the point where the femur broke. ....	52
<b>Figure 20:</b> Example of bone callus representation concerning the plate position into the complete model. The main axes of the Local Cylindrical-coordinate correspond to the absolute coordinate represented in the Figure.....	54
<b>Figure 21:</b> Logarithmic Strain contour maps for 1 mm of fractured gap and 60 MPa of callus tissue Elastic Modulus. Focus on the three main <i>axial components</i> in a Local Cylindrical System (LCS). ....	56
<b>Figure 22:</b> Logarithmic Strain contour maps for 1 mm of fractured gap and 60 MPa of callus tissue Elastic Modulus; focus on the three main <i>tangential components</i> in a local cylindrical system (LCS).....	56
<b>Figure 23:</b> Global Stress contour maps for 1 mm of fractured gap and 60 MPa of callus tissue Elastic Modulus; focus on the three main <i>axial and tangential components</i> in a local cylindrical system (LCS). ....	57
<b>Figure 24:</b> Logarithmic Strain maps for 3 mm of fractured gap and 60 MPa of callus tissue's Elastic Modulus. Focus on three main <i>axial and tangential components</i> in local cylindrical coordinates.....	59
<b>Figure 25:</b> Logarithmic Strain maps for 5 mm of fractured gap and 60 MPa of callus tissue's Elastic Modulus. Focus on three main <i>axial and transversal components</i> in local cylindrical coordinates.....	60
<b>Figure 26:</b> Global Stress maps for 3 mm of fractured gap and 60 MPa of callus tissue's Elastic Modulus. Focus on three main <i>axial and transversal components</i> in local cylindrical coordinates.....	61
<b>Figure 27:</b> Global Stress maps for 5 mm of fractured gap and 60 MPa of callus tissue's Elastic Modulus. Focus on three main <i>axial and tangential components</i> in local cylindrical coordinates.....	62
<b>Figure 28:</b> Logarithmic Strain contour map for 1 mm of fractured gap and an increased callus tissue's Elastic Modulus. Focus on the three main <i>axial and tangential components</i> in local cylindrical coordinates for the <i>Traditional Static Plate</i> . ....	63
<b>Figure 29:</b> Logarithmic Strain contour map for 1 mm of fractured gap and increased callus tissue's Elastic Modulus. Focus on the three main <i>axial and tangential components</i> in local cylindrical coordinates for the <i>Dynamic Plate in the Locked configuration</i> . ....	64

<b>Figure 30:</b> Logarithmic Strain contour map for 1 mm of fractured gap and increased callus tissue's Elastic Modulus. Focus on the three main <i>axial and tangential components</i> in local cylindrical coordinates for the <i>Dynamic Plate</i> in the <i>un-locked configuration</i> . .....	65
<b>Figure 31:</b> Logarithmic Strain's <i>maximum</i> and <i>minimum</i> values for the <i>Traditional Static Plate</i> . Focus on the three main <i>axial and tangential components</i> in a global coordinates system for an increased fracture gap (1 to 5 mm) and a fixed Elastic Modulus of 60 MPa. ....	68
<b>Figure 32:</b> Logarithmic Strain's <i>maximum</i> and <i>minimum</i> values for the <i>Wireless Dynamic Plate</i> in a <i>Locked</i> configuration. Focus on the three main <i>axial and tangential components</i> in a global coordinates system for an increased fracture gap (1 to 5 mm) and a fixed Elastic Modulus of 60 MPa.....	69
<b>Figure 33:</b> Logarithmic Strain's <i>maximum</i> and <i>minimum</i> values for the <i>Wireless Dynamic Plate</i> in an <i>Un-Locked</i> configuration. Focus on the three main <i>axial and tangential components</i> in a global coordinates system for an increased fracture gap (1 to 5 mm) and a fixed Elastic Modulus of 60 MPa.....	70
<b>Figure 34:</b> Logarithmic Strain's <i>maximum</i> and <i>minimum</i> values for the <i>Traditional Static Plate</i> . Focus on the three main <i>axial and tangential components</i> in a global coordinates system for a fracture gap of 1 mm and an increased callus tissue's Elastic Modulus (from 60 to 600 MPa). .....	71
<b>Figure 35:</b> Logarithmic Strain's <i>maximum</i> and <i>minimum</i> values for the <i>Wireless Dynamic Plate</i> in a <i>Locked</i> configuration. Focus on the three main <i>axial and tangential components</i> in a global coordinates system for a fracture gap of 1 mm and an increased callus tissue's Elastic Modulus (from 60 to 600 MPa). .....	72
<b>Figure 36:</b> Logarithmic Strain's <i>maximum</i> and <i>minimum</i> values for the <i>Wireless Dynamic Plate</i> in an <i>Un-Locked</i> configuration. Focus on the three main <i>axial and tangential components</i> in a global coordinates system for a fracture gap of 1 mm and an increased callus tissue's Elastic Modulus (from 60 to 600 MPa). .....	73
<b>Figure 37:</b> Traditional plate <i>von Mises Stress (MPa)</i> increases the initial gap. Focus on the main plate body and the most solicited screw hole. ....	74
<b>Figure 38:</b> Projected dynamic plate <i>von Mises stress (MPa)</i> by increasing the initial gap. Focus on the main plate body and the most pin section. ....	75
<b>Figure 39:</b> Von Mises stress (MPa) on the bone tissue due to initial contact between the two fractured bones. A comparison between the traditional Static Plate and the projected Dynamic Plate in the locked condition has been made....	75

# List of Tables

Table 1. Analytical calculation of the equivalent loading forces using the half sigma failure and the pin diameter as input data by Jourawski approximation. ....	17
Table 2. Primary data of manufactured feasible springs obtained from the spring design program based on German Standard Spring.....	19
Table 3. The physical meaning of ADAMS/Solver variables.....	28
Table 4. Range of parameterized values, according to physical springs and primary geometry involved in the concept phase .....	29
Table 5. Details of the Mesh and Material parameters for each component model into the FE model.....	34
Table 6. Main parameters to be defined in the model for the standard pressure-overclosure formulation with exponential definition.....	36
Table 7. Detail of the two contact parameters simulated into the FE model. .	36
Table 8. Main Elastic Modulus for a referenced fracture healing process.....	41
Table 9. Details of loading conditions were analyzed for the fracture healing studies. ....	42
Table 10. Classification of IFS axial and shear ranges according to literature. ....	55



# **Chapter 1**

## **Introduction**

---

The main clinical problem and thesis aims and objectives are here introduced.

## **1.1 Main clinical problem**

The primary purpose of a medical device for fracture treatments is to ensure stable support to the bone during the healing phase, allowing the patient to walk as soon as possible (Taljanovic et al., 2003). Lower limb fracture incidence has been estimated to reach about 300'000 cases per year in the United States alone due to high-energy impacts or a fall from height (Gulati et al., 2012; Otte, D.\*; Haasper, 2017). The treatment of severe fractures in poly-traumatized patients, possibly with the potential compromise of vital functions or significant bone consolidation delays, has gained more attention due to difficulties of intervention within a single surgery (Larsson et al., 2001).

## **1.2 Aims and objectives**

The new concept of internal fixation needs to consider some peculiarities compared to a traditional static plate, which are:

- the new plate is made of two parts, sliding each other, which respective interactions must be studied;
- energetic and geometric specifications, such as the maximum energy demand and limited device size, need to be considered during the whole design process;

- the uncertainty of physical parameters must be included in the design, i.e., the friction of materials to be posed in contact and the spring's pre-load for discharging the pin.

Numerical stress analysis must be performed to define a reference geometry complying with existing osteosynthesis device regulation (EU 2017/745) and experimental tests to evaluate the structural response in a realistic environment (Yaneva-Deliverska et al., 2015). Furthermore, the conceived prototypes must be produced according to an approved company process flow following ISO 13485:2016 (Zyga, 2011). In this framework, the introduced dynamization system has been developed to treat polytraumatized patients, who would benefit from the fast recovery guaranteed by a minimally invasive technique and eliminate the need for a new intervention.

# **Chapter 2**

## **State-of-the-art**

---

This chapter introduces state-of-the-art fracture healing and the main strategies adopted to dynamize fracture and improve the fracture healing process.

## 2.1 Fracture healing studies

There are two principal types of fracture healing:

- (1) **Direct bone repair**, which comes from osteonal remodeling under a rigid fracture stabilization, and can occur with little or no external callus formation (Perren, 2002);
- (2) **Indirect bone repair** (secondary fracture healing) comes from endochondral healing at the fracture gap or intramembranous ossification site within the periosteum when a small degree of movement occurs under less rigid IFS stabilization (Giannoudisa & \*, Thomas A. Einhornb, 2011; Perren, 2002).

### 2.1.1 Mechanical factors influencing the fracture gap

Some forerunner studies in the field have concluded that fundamental factors involved in the fracture healing process are the following: (1) the *gap size*, (2) the amount of interfragmentary strain (*IFS*), and (3) the hydrostatic pressure along the calcified surface (Augat et al., 1998; Lutz E. Claes et al., 1998). In particular, considering the first study, the increase of the fracture gap has resulted in inferior mechanical and histological properties; the smaller *IFS* could already stimulate the secondary fracture healing, while its higher value did not affect the repair process or have any stimulatory effect (Augat et al., 1998). The second study

affirms that slight hydrostatic pressure and *IFS* ( $<0.15 \text{ MPa}$ ;  $<5 \%$ ) supported the intramembranous bone formation, while more considerable *hydrostatic pressure* and *IFS* ( $>0.15 \text{ MPa}$ ;  $5\text{-}15 \%$ ) supported endochondral ossification (Lutz E. Claes et al., 1998).

### **2.1.2.1 The influence of axial and shear component**

According to Perren studies, the optimal value to stimulate fracture healing should be between 2 and 10 % of *IFS* concerning axial load (Perren, 2002). Nevertheless, other authors have hypothesized that type of *IFS* along with the fracture healing site directly influence the vascularisation of that site; in particular, they affirm that under **compressive strain**, the neo-formed flexible vessels do not transfer significant load between the weak endothelial cell junctions and immature mural structures, reducing vessel rupture risk, while both **tensile** and **shearing deformations** result in disruptive loads despite a biochemically angiogenic environment (L. E. Claes & Meyers, 2020). Other authors demonstrated the same hypothesis by conducting an experimental study on ten skeletally mature merino sheep. The right tibia was cut with a mid diaphyseal osteotomy with 3 mm of the interfragmentary gap, stabilized by a custom-made external fixator (Park & Augat, 2004). All those studies confirm that fixation allowing excessive shear movement significantly delayed the healing of diaphysis osteotomies.

### **2.1.2 Different types of fracture treatments**

Internal stabilization with inter-fragmentary compression through screws and plates guarantees absolute stability, bringing bone to direct healing (Taljanovic et al., 2003). Fracture immobilization with nailing or a bridge plate provides less rigid fixation and excellent support for the bones' consolidation through callus formation via indirect healing (Bottlang et al., 2016; Henschel et al., 2017). Internal stabilization has recently gained more attention because of the less invasive surgery and better patients' comfort with external fixation methods (LE E. Claes et al., 1995). The bridge plate technique is well indicated for comminuted long bone fractures affecting the proximal or distal growth area since the intervention can be done with a minimally invasive technique and a percutaneous approach. This procedure significantly reduces the tissue's stress during surgery for poly-traumatized patients with significant lower limb problems (Sonderregger et al., 2010).

### **2.1.3 Numerical modeling of the secondary fracture healing**

Another exciting aspect of the process is the dynamics of secondary fracture healing. In particular, some authors decided to develop an integrated numerical model of the fracture gap calibrated with in-vivo studies, to quantify the influence of the different loads on the optimal fracture healing process; the algorithms were

based on distortional strain alone or in combination with dilatational strain or fluid velocity (Steiner et al., 2013, 2014a, 2014b).



## 2.2 Dynamization systems

Dynamization of fracture fixation is a vital strategy to reduce recovery time for a patient (Larsson et al., 2001; Yamaji T et al., 2001). The principal aim of this treatment is to stimulate the proliferation of callus in the early phase of recovery and accelerate the new bone formation (Foxworthy & Pringle, 1995). External stabilization is a standard gold technique for this type of treatment, but internal fixation has recently gained increasing attention (LE E. Claes et al., 1995).

### 2.2.1 The mechanotransduction process

One of the fundamental concepts in orthopedics is that the healing of fractures can be accelerated or decelerated depending on the most appropriate loading condition exerted on the fracture gap (Ghiasi et al., 2017; Glatt et al., 2017). In literature, this phenomenon is recognized as **mechano-transduction** and is based on adapting the bone tissue to the external mechanical environment, which can occur in response to static and dynamic loads (Hannouche et al., 2001). The relationship between the structure and function of bone is described by Wolff's Law which based observation on comparing the stress trajectories in Culmann's crane with the pattern of trabecular bone in the femoral neck; however, the analysis he conducted was based on a misinterpretation of the mechanical data and the rejection of the bone resorption process (Wolff & Wolff, 1986). The first

author that accurately describes the process of adapting the bone to dynamic loads was Wilhelm Roux in 1885, influenced by Darwin and Wallace's functional adaptation principles (Lee, 1999).

### **2.2.2 In-vivo monitoring of callus stiffness**

A critical aspect to consider in the dynamization process is the physical measure of callus stiffness. It is unclear which mechano-sensitive phases and mechanical stimulation are required throughout the repair (Einhorn & Gerstenfeld, 2015; Giannoudis & \*, Thomas A. Einhorn, 2011; Glatt et al., 2017; Salisbury Palomares et al., 2009), and some authors have developed sophisticated physical devices to monitor callus stiffness over time (Barcik et al., 2021; Bishop et al., 2003; Blázquez-Carmona et al., 2020; Tufekci et al., 2018). A two degrees-of-freedom external fixator has been developed to control IFS movements over an ovine tibial osteotomy investigating the mechano-transduction mechanisms in fracture healing controlling IFS strain magnitudes and measuring stiffness over the gap (Bishop et al., 2003). Other authors developed a dynamic fixator to investigate if stimulation limited to the early proliferative phase is sufficient for bone healing, obtaining good results (Tufekci et al., 2018). A programmable active fixation system for systematic in-vivo investigation of the bone healing process has been lately developed starting from this prototype. The device joined the ability to precisely control the mechanical condition that acts within a fracture,

with continuous monitoring of the system's healing progression and autonomous operation throughout the experiment, resulting in a significant advantage in assessing the clinical efficacy of pre-defined protocols (Barcik et al., 2021). Some other authors developed an external fixator capable of adapting to multiple bone regeneration processes following those principles. The measurements are conditioned and subsequently sent wirelessly to a PC to be displayed and analyzed in vivo, using a real-time monitoring application (Blázquez-Carmona et al., 2020). Such systems give new inputs to the study of the fracture healing process, especially in defining new clinical protocols to improve the fracture repair processes.

### **2.2.3 Loading frequency and peak strain magnitude**

More generally, *amplitude*, *frequency*, and *shape* are three factors that can influence a mechanical stimulus. Some authors focused their analysis on the peak strain magnitude and the loading frequency, finding that even a short exposure to functional loading is enough to produce a substantial architectural modification (Clinton T. Rubin and Lance E. Lanyon, 2002). Strain sensitivity seems to be the main parameter involved in bone remodeling, while total strain cycles and respective amplitude are small enough to exclude fatigue damage (Clinton T. Rubin and Lance E. Lanyon, 2002). The low intra-cortical remodeling levels, which drive large formation on the bone surfaces, confirm this thesis (Clinton T.

Rubin and Lance E. Lanyon, 2002). In contrast, the bone appears to have no adaptive mechanism in advance to prolong fatigue life by reducing functional strains in response to the number of strain cycles to which it is being subjected (Clinton T. Rubin and Lance E. Lanyon, 2002). Some earlier experiments suggest that no additional increase in bone mass occurs when the number of load cycles is increased (Goodship et al., 2009). Some other authors focused their attention on the recovery period after a single pulse, which may influence the efficacy of post-operative management and physiotherapeutic intervention (Hente & S.M., 2018), finding new exciting hypotheses that can drive new research and studies.

# Chapter 3

## Conceptual phase

---

This chapter introduces the rationale behind realizing the first plate concept and his manufacturing flow's consequent setting. The specific case concerns analyzing a projected geometry composed of some interacting parts, which movement should be generated by a preselected motor unit. Datasheet limitations for the power and force must be considered to have a functional and well-integrated system. Furthermore, geometrical and mechanical considerations on physical components like the spring or the friction values must be considered to choose an appropriate range of values for the parameters involved in the multi-body analysis.

### 3.1 Mechanical plate interactions

The wireless dynamic plate will consist of two main components:

- (1) The *main body*, fixable to the bone using angular stability screws, which contains both the housing for the actuating system for dynamizing the plate and the locking/unlocking system;
- (2) The *guide*, within which the main body can slide for a bit of stroke, is coupled to the main body only using the locking/unlocking system; the guide is also fixed to the bone by angularly stable screws.

In the locked configuration, the main body and the guide are firmly connected through the locking device, highlighted in *Figure 1* as the pin's lateral piece. Conceptually, the main body and the guide can slide each thanks to a prismatic coupling that guarantees the transmission of flexural and torsional load loads between those two parts, avoiding the axial load transmission when the pin is not inserted into the guide hole. The pin's third party can slide in the horizontal direction (*Figure 1, arrow 2*) thanks to the passive action of a mechanical spring, realizing the “dynamic” unlocked configuration when the specific inclined plane is retracted by the actuation mechanism (*Figure 1, arrow 1*).

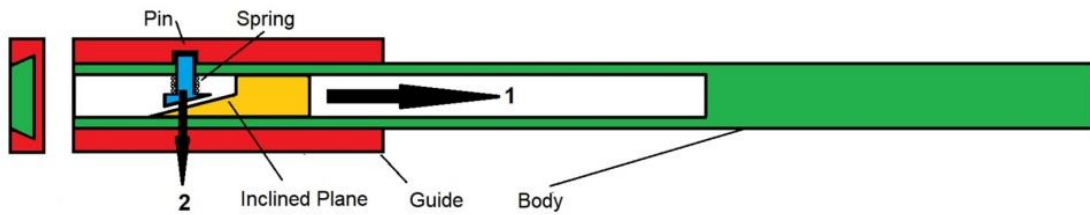


**Figure 1:** Conceptual design of the plate dynamization system.

### 3.1.1 Design of the un-locking geometry

A simple mechanism has been designed as the primary physical constraint between the guide and the main plate body. The mechanism comprises two metallic parts that can slide one concerning the other:

- (1) the *pin*, a triangular base with a circular extension;
- (2) the *inclined plane*, a rectangular block with a triangular part that perfectly matches the previous one.

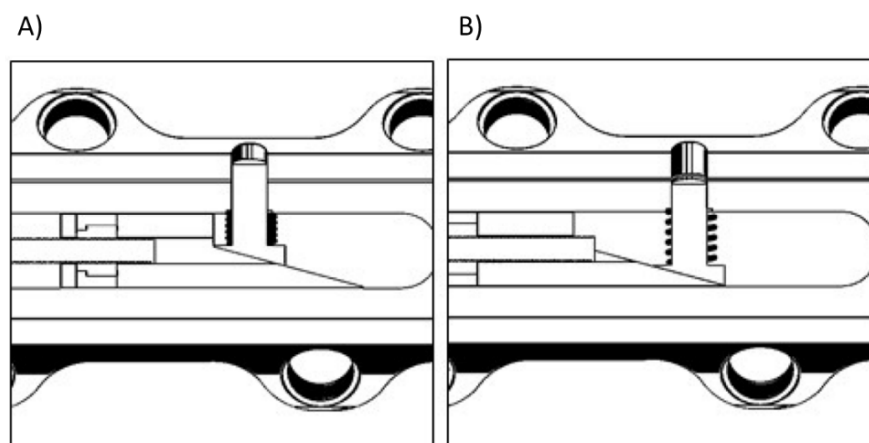


**Figure 2:** Detail the unlocking mechanism in locked (A) and unlocked (B) configuration.

The slope angle of this system is a fundamental aspect of the unlocking principle since it is a function of the friction coefficient related to the surfaces, as highlighted next:

$$F_a = F_n * \mu = K_p * \cos(\varphi) * \tan(\varphi) = K_p * \sin(\varphi) = F_p \quad (1)$$

Where:  $F_a$  is the friction force parallel to the plane;  $F_n$  is the component of the force, normal to the plane;  $\mu$  is the friction coefficient between the surfaces;  $F_p$  is the component of the force, parallel to the plane;  $K_p$  is the spring pre-load, and  $\varphi$  is the inclination angle of the pre-defined geometry. As we can see from equation (1), selecting an angle of inclination equal to the friction angle, i.e., choosing a value of  $\mu = \tan(\varphi)$ , the relation becomes an identity the force resultant on the block will be close to zero.

### 3.1.2 Pin shear section: force evaluation

Conceptually, the *pin* is the only piece that guarantees the structural continuity between the different parts composing the plate. The primary function of the pin is to avoid any reciprocal sliding between the two separated mechanical parts fixed by the bone, i.e., the *main body* and the *guide*. When the plate is implanted into the body, in the static mode, it needs to resist the worst axial loads acting by the plate in the most frequent daily activities (Morlock et al., 2001). Since the most solicited section is the one that stays between the guide and the



main body and is subjected to shear force, the Jourawski formula represents an excellent analytic method to derive its minimum diameter: this was derived looking at the equivalent forces that a specific diameter can resist, once specified the sigma failure of the constitutive material (*Table 1*).

**Table 1.** Analytical calculation of the equivalent loading forces using the half sigma failure and the pin diameter as input data by Jourawski approximation.

Jourawski: Equivalent Force on pin section (N)			
Sigma failure (N/mm <sup>2</sup> )	Diameter (mm)	Circular section	Rectangular section
≈ 425	2.0	1000.0	1131.8
	2.5	1562.5	1768.4
	3.0	2250.0	2546.5
	3.5	3062.5	3466.1
	4.0	4000.0	4527.1

### 3.1.3 Spring action: physical evaluation

To select feasible springs which are physically realizable, two parameters of primary interest considered were:

- (1) the *minimum section* of the *pin* that can resist structural loads;
- (2) the *maximum dimension* of the *internal chamber* able to integrate the actuation system.

The spring design program used for this calculation is based on the German standard for springs and a specific experience in production engineering. Material,

quality category as per DIN EN 15800, and a valid combination of diameter, spring forces, spring deflections, and lengths must be entered in the parameter pre-settings (Gutekunst & Co., n.d.). As a result, by selecting the specific dimension tolerances and the material properties, three different springs have been analyzed and outlined in *Table 2*, highlighting the parameters of interest for the multi-body analysis.

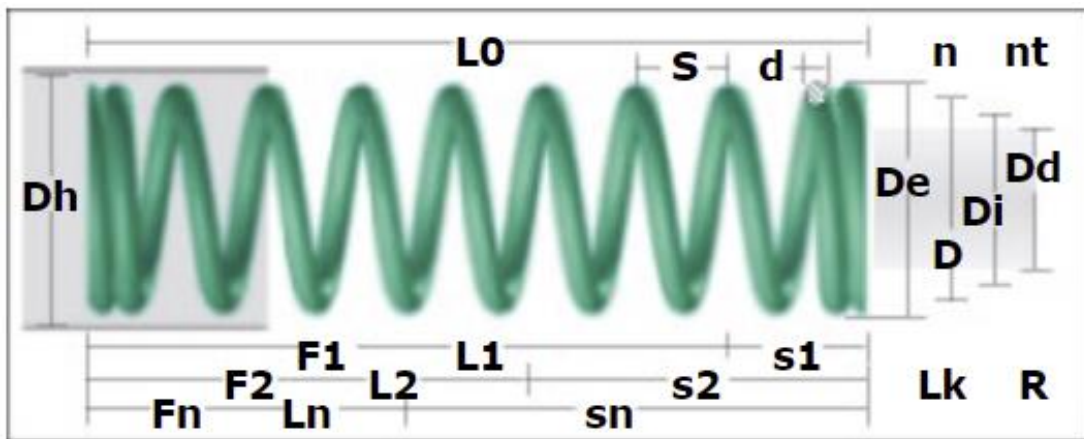


**Figure 3:** Main parameters for the calculation of the spring pre-setting.

**Table 2.** Primary data of manufactured feasible springs obtained from the spring design program based on German Standard Spring.

Data	Parameter	#01: light	#02: intermediate	#03: stiff
<b>MECHANICAL</b>	<b>Shearing Modulus (N/mm<sup>2</sup>)</b>		<b>81500</b>	
	<b>Elasticity Modulus (N/mm<sup>2</sup>)</b>		<b>206000</b>	
	Minimum Tensile Strength (N/mm <sup>2</sup> )	2395.3	2342.4	2296.6
	Permitted shearing strength (N/mm <sup>2</sup> )	1197.6	1171.2	1148.3
	Stress coefficient (/)	1.190	1.226	1.250
	<b>Spring rate (N/mm)</b>	<b>5.166</b>	<b>14.357</b>	<b>21.435</b>
<b>GEOMETRICAL</b>	<b>Wire diameter (mm)</b>	<b>0.60</b>	<b>0.70</b>	<b>0.80</b>
	<b>Inner coil diameter (mm)</b>	<b>3.80 ± 0.10</b>	<b>3.70 ± 0.10</b>	<b>3.80 ± 0.10</b>
	Mean coil diameter (mm)	4.40 ± 0.10	4.40 ± 0.10	4.60 ± 0.10
	Outer coil diameter (mm)	5.00 ± 0.10	5.10 ± 0.10	5.40 ± 0.10
	Maximum diameter of the mandrel (mm)	3.50	3.40	3.50
	Maximum diameter of the bush (mm)	5.48	5.62	5.91
<b>LENGHT</b>	Length of unstressed spring (mm)	7.00 ± 0.17	6.00 ± 0.12	6.00 ± 0.12
	<b>Length of spring at F1 (mm)</b>	<b>4.00</b>	<b>4.20</b>	<b>4.20</b>
	<b>Length of spring at F2 (mm)</b>	<b>3.50</b>	<b>3.60</b>	<b>3.70</b>
	<b>Length of spring at Fn (mm)</b>	<b>3.33</b>	<b>3.02</b>	<b>3.44</b>
	Block length (mm)	3.00	2.80	3.20
<b>DEFLECTIO N</b>	<b>Spring deflection at F1 (mm)</b>	<b>3.00</b>	<b>1.80</b>	<b>1.80</b>
	<b>Spring deflection at F2 (mm)</b>	<b>3.50</b>	<b>2.40</b>	<b>2.30</b>
	<b>Spring deflection at Fn (mm)</b>	<b>3.67</b>	<b>2.98</b>	<b>2.56</b>

	Spring deflection to block (mm)	4.00	3.20	2.80
<b>FORCES</b>	Prestressed spring force: F1 (N)	15.50 ± 1.02	25.84 ± 1.97	38.58 ± 2.84
	Loaded spring force: F2 (N)	18.08 ± 1.04	34.46 ± 2.05	49.30 ± 2.94
	Maximum force in static use: Fn(N)	18.99	42.74	54.89
	Theoretic maximum force at Block length (N)	20.67	45.94	60.02
<b>TEST</b>	Test force for R: 0.3*Fn (N)	5.70	12.82	16.47
	Test force for R: 0.7*Fn (N)	13.29	29.92	38.42
<b>COIL</b>	Active coils (/)	3	2	2
	Total coils (/)	5	4	4
	Number of non-elastic coils (/)	2	2	2

## 3.2 Electrical parts integration

The electrical part is an essential step of the prototyping phase since they need to be integrated inside the plate. The bending rigidity of the plate dramatically depends on the main transversal section along which the plate-bone system is bent (Gautier et al., 2001), which in this case is limited by the geometrical dimension of the actuation part, which will be selected to move the locking/unlocking mechanisms.

### 3.2.1 Actuation system integration

A motor actuation system has been selected for the wedge-shaped block actuation and relative movements. A specific combination has been selected for the actuation part of the un-locking mechanism, considering both the locking and un-locking phases. It is composed of three sub-blocks which are: (1) a *DC motor*; (2) a *planetary gear's* reduction mechanism, which can have from 1 to 5 *stages* of reduction depending on output torque and velocity; (3) a *metric screw drive*, which can have different lengths and type of nuts, depending on the efficiency needed by the specific application. The combination selected has been the following:

- A Motor Unit, the *RE6 DC*, with  $\Phi = 6 \text{ mm}$ , precious metal brushes, 0.3 W of nominal power, and 4.5 V of nominal tension;

- A Planetary gearhead, the *GPS6 screwdriver*, with  $\Phi = 6 \text{ mm}$ , four reduction stages, and a metric lead screw with a standard length of  $45 \text{ mm}$ .

The main advantages of brush motors are their relative cheapness compared to the brushless ones, the easy control, and the prompt response to commands at low revs or stationary.



**Figure 4:** The metal brush motor with the four stages gear reduction system and the preselected screw drive in the assembled configuration.

### 3.2.2 Magnetic power supply

An inductive power transfer system has been adopted to give the necessary power supply, consisting of two magnetically coupled coils. The related power is transferred from the transmitting to the receiver side, implementing a specific electrical circuit that maximizes the power transfer (Fadhel et al., 2019). The actuation part needs a voltage supply of  $4.5 \text{ V}$  from the internal supply circuit in a continuous mode, and the fundamental electrical components needed for the implementation of the power transfer circuit are:

- A transmitter and receiver coil;

- Two or more capacitors to set the resonance condition;
- One voltage supply for the transmitter side.

One of the main design constraints to consider must be the size and geometry of the *receiver coil*, which should be small enough to be hosted on the plate yet big enough to receive enough power to supply the motor. Moreover, additional components might be necessary to convert voltages from DC to AC on the transmitter side – and vice versa on the receiver side – making the power transfer work properly (Fadhel et al., 2019). Finally, for safe feedback to the medical doctor, it might be worth considering a feedback element that can sense if the pin has completed its motion – e.g., a switch that closes at the pin motion end.

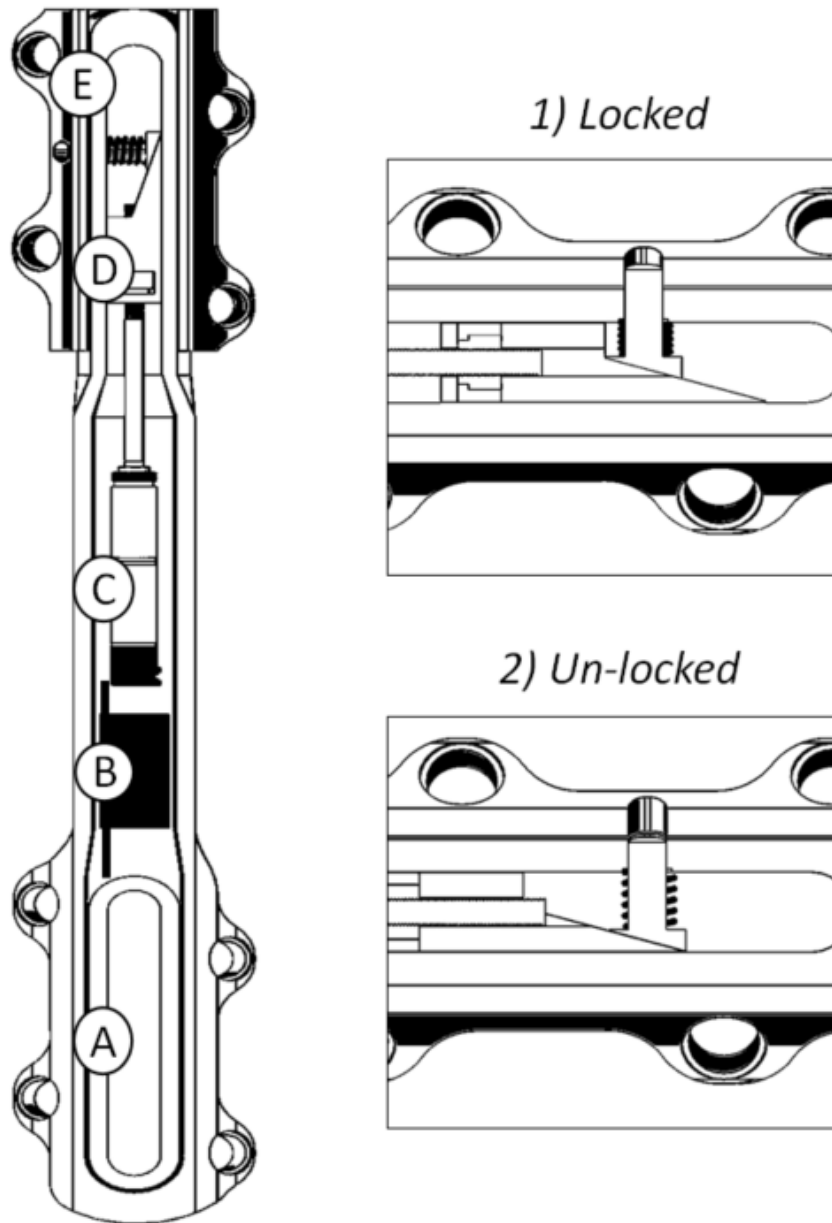


**Figure 5** Left image: detail of the internal actuation system of the plate: A) pin; B) wedge-shaped block; C) brush motor; D) receiver circuit; E) receiver coil. Right image: Detail the locking mechanism in the locked (1) and un-locked (2) configurations.



### 3.3 Setup of the manufacturing flow

After analyzing all the parts, a first design concept of the plate has been realized, as highlighted in *Figure 5*. Once the component has been designed in detail, the respective manufacturing flow had to be set up, according to Medical Device Regulation (EU) 2017/745 for medical devices (Clinton T. Rubin and Lance E. Lanyon, 2002). Its main steps have been the following ones:

- Step 1: Sourcing of raw materials;
- Step 2: Machine Processing: folding, milling, drilling, threading, wire erosion; Roughing, Burr removal; Washing; Packaging in labeled bags;
- Step 3: Acceptance Check;
- Step 4: Acceptance; Belt Sanding; Polishing; Washing; Final check; Packaging, shipping;
- Step 5: Solvent washing; Sandblasting; Quality Control (QC), single packaging in plastic trays;
- Step 6: Acceptance Check;
- Step 7: Marking; Washing; Preliminary packaging (Clean Room ISO 7 Operational);
- Step 8: Sterilization;
- Step 9: Acceptance check;
- Step 10: Final packaging and labeling; Release.

## **Chapter 4**

# **Numerical and experimental strategies**

---

This chapter introduces numerical and experimental methods adopted to obtain the first physical prototype. The MB analysis has been used to analyze the actuation unit's consumption. In contrast, the FE method has been used to fasten the experimental certification procedure and evaluate the fracture healing process of the projected plate concerning a traditional static plate.

## 4.1 Multi-body method

A multi-body method is a numerical approach for mechanical analysis when several parameters (both mechanical and electrical) are involved in the system's dynamics or kinematics. The Euler-Lagrange equation represents a general multi-body system:

$$\frac{d}{dt} \left( \frac{\partial L}{\partial \dot{\mathbf{q}}} \right) - \frac{\partial L}{\partial \mathbf{q}} + \mathbf{\Phi}_q^T \lambda = \mathbf{Q} \quad (2)$$

where  $L$  is the Lagrangian equation of the system, given by the difference between the kinetic and potential equation of a rigid body,  $\mathbf{q}$  is the vector of generalized coordinates, while  $\lambda$  contains the Lagrange multipliers, referred to as binding reactions. The constraint equations are contained in  $\mathbf{\Phi}$ , and the parameter

$$\mathbf{\Phi}_q = \frac{\partial \mathbf{\Phi}}{\partial \mathbf{q}}$$

Represent the Jacobian matrix of constraints.  $\mathbf{Q}$  is a vector representing the externally applied forces, balanced by the acceleration, the potential force, and Lagrange multipliers. In particular, the algorithm used by *ADAMS/Solver* implements the following equation (Collingridge *et al.* 2014a, 2014b):

$$M\ddot{\mathbf{q}} + M\dot{\mathbf{q}} - \frac{1}{2}\dot{\mathbf{q}}^T \frac{\partial M}{\partial \mathbf{q}} \dot{\mathbf{q}} + \frac{\partial V}{\partial \mathbf{q}} + \mathbf{\Phi}_q^T \lambda = \mathbf{Q} \quad (3)$$

Considering  $n$  differential second-order equations and  $m$  constraint equation for which the meaning of each component is explained in *Table 3*.

**Table 3.** The physical meaning of ADAMS/Solver variables

<i>Equation's variable</i>	<i>Physical meaning</i>
$n$	Number of bodies
$M$	Mass matrix: $n \times n$
$\frac{1}{2} \dot{q}^T \frac{\partial M}{\partial q} \dot{q}$	Total kinetic energy
$V$	System potential energy
$\Phi_q$	Jacobian constraint matrix : $m \times n$
$Q$	Applied Force column vector: $n \times 1$

#### 4.1.1 Modeling the un-locking mechanism

According to the conceived conceptual design, the multi-body model has been built in ADAMS View (2019, MSC Software, Santa Ana, CA, USA). The essential components have been modeled and then parameterized according to main physical characteristics, and considering the following conditions:

- the pin and the inclined plane can translate axially, and specific friction has been attributed to this movement;
- the main body and the pin's head have been modeled by solid parametrical geometry; hard contact has been defined to simulate the metallic behavior between the two faces; the impact formulation has been defined with high stiffness and low damping ( $k = 10E+5 \text{ N/mm}$ ;  $c = 10 \text{ N}\cdot\text{s/mm}$ );

- the relative motion has been defined for the main body to simulate the motor unit's input with a prescribed sinus function of  $x(t) = 5 \cdot \sin(\pi/2 \cdot t)$  to give a complete movement cycle along with the pin.

A specific range of parameters is selected for the study, as highlighted in *Table 4*, where the two main outputs have been the maximum force and power required to discharge the conceived unlocking mechanism. The latter has been calculated by multiplying the horizontal translation speed ( $v$ ) with the measured force ( $F$ ), following this equation:

$$P = \frac{L}{\Delta t} = F \cdot \frac{s}{\Delta t} = F \cdot v$$

**Table 4.** Range of parameterized values, according to physical springs and primary geometry involved in the concept phase

	<i>Variable</i>	<i>Range of values</i>
<b>INPUT DATA</b>	Plane Inclination [°]	9° - 18°
	Friction Coefficient [/]	0.15 - 0.60
	Spring Pre-load [N]	20 - 80
	Spring Stiffness [N/mm]	5 - 20
<b>OUTPUT DATA</b>	Maximum Force [N]	/
	Maximum power [mW]	/

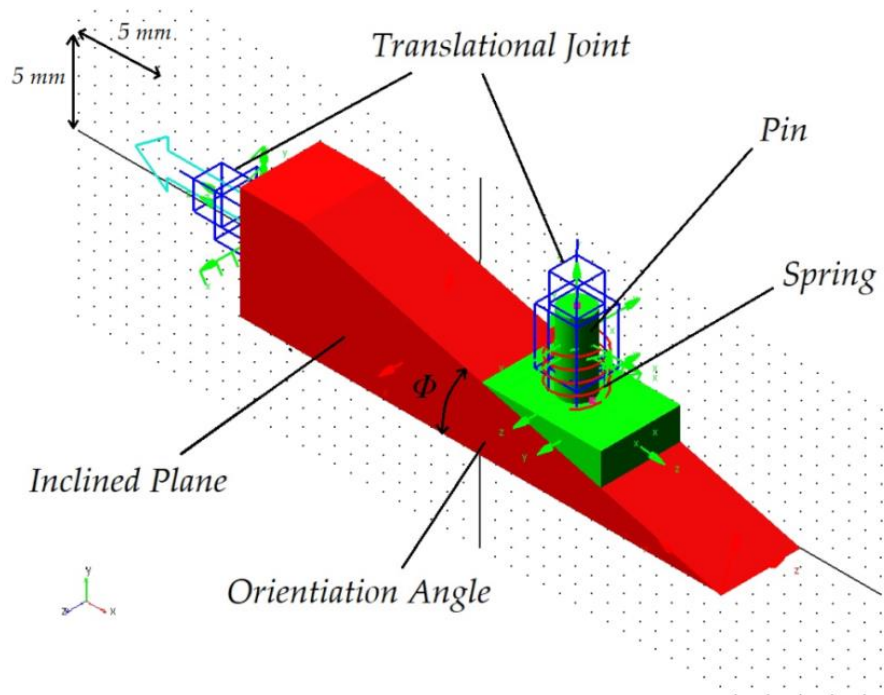


**Figure 6:** Multi-body model of the un-locking mechanism with an overview of its principal components.

## 4.2 FE analysis for certification purposes

The simulation of the *ASTM F382.17* regulation can represent a fundamental step for simplifying the certification procedure. The study of the plate's flexural stiffness and fatigue bending limit required modeling the whole integrated CAD geometry (*Figure 7*).

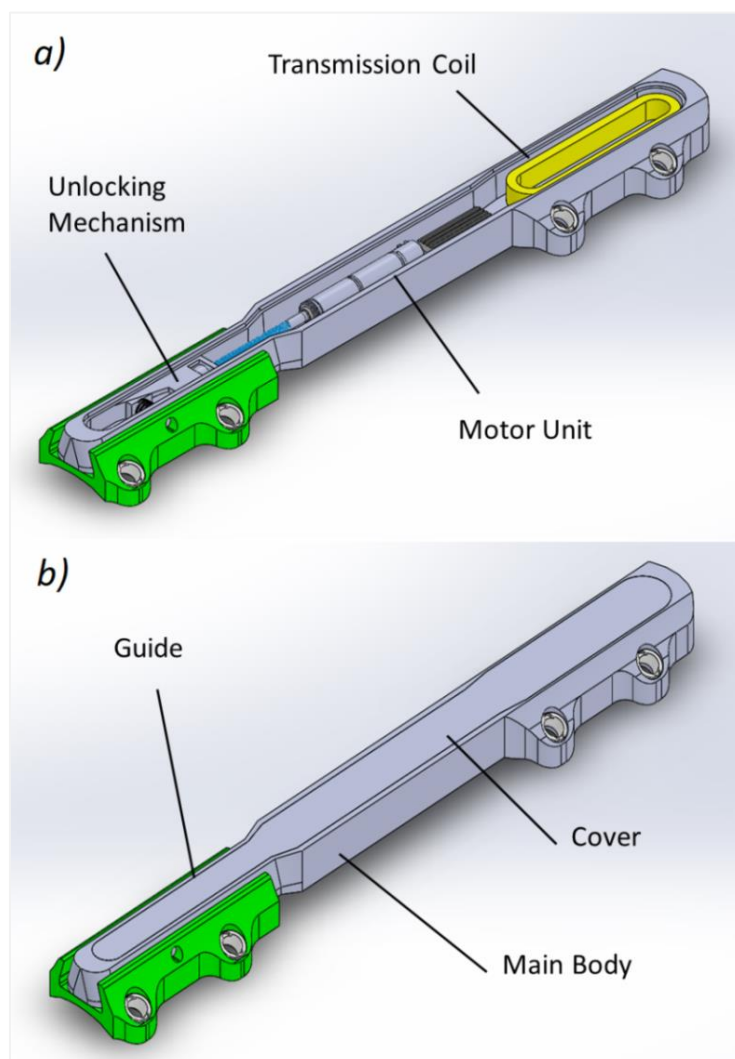


**Figure 7:** Refined plate design: internal components (a) and external parts (b).

### 4.2.1 Full setup and boundary conditions

The model represented in *Figure 8* has been obtained with the mesh discretization of the optimized CAD geometry represented in *Figure 7*. The software used for the FE model generation and primary interaction setting has been ANSA (Beta CAE system). The model created has been simulated with Abaqus CAE (2018, Dassault Systemes, Vélizy-Villacoublay, FR), a widespread code used in the biomedical field.

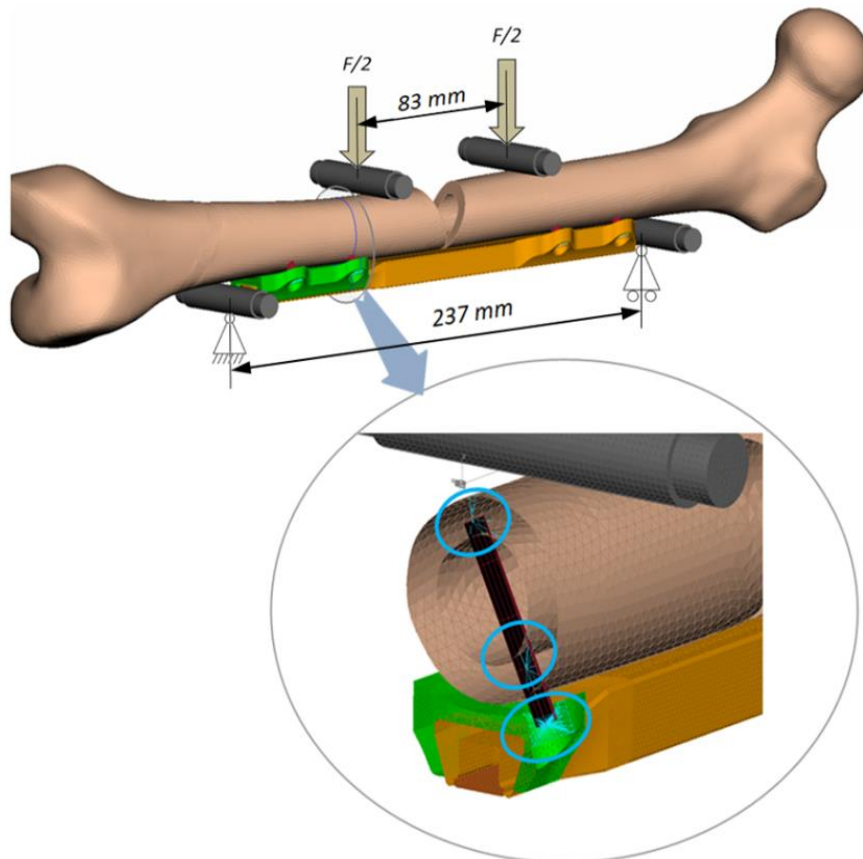


**Figure 8:** The FE model, according to the overall setup, indicates the respective loads and boundary constraints; one screw section model has been highlighted in the circle below.



## 4.2.2 Mesh and material properties

The geometry has been discretized into *3D tetra elements*, considering an appropriate element size for every structure, and a spread elements size for the femur and the rollers (*Table 5*), which have been modeled as follows:

- The femur (Sawbones®, Europe AB, Malmö, Sweden) meshed with *3D tetra elements*, with diaphyseal fracture as prescribed by regulation;
- Four metallic rollers (having a *25 mm* radius) were modeled with *2D shell elements* and positioned precisely in contact with the femur, as the experimental loading setup prescribed.

The *AISI 316LVM* with an elastic modulus equal to *187.5 GPa* and 0.3 Poisson's ratio has been used for plate components. The non-structural Sawbones® material, with *0.6 GPa* of elastic modulus and 0.3 of Poisson's ratio, was assigned to the femur, and the Stainless Steel material, with *210 GPa* of elastic modulus 0.3 of Poisson's ratio, was assigned to the screws and rollers. A linear and isotropic behavior has been considered for all the analyses. The screws have been modeled with multiple 1D beam elements (with a *3.5 mm* radius), connected to the bone structures by rigid kinematic joints (RBE2), as shown in *Figure 8*.

**Table 5.** Details of the Mesh and Material parameters for each component model into the FE model.

<b>Component name</b>	<b>Type of Element</b>	<b>N° of Elements</b>	<b>Mesh size [mm]</b>	<b>Material</b>
<i>Main Body</i>	3D Tetra4	415,456	0.3 – 0.8	AISI 316LVM
<i>Guide</i>	3D Tetra4	134,410	0.3 – 0.8	AISI 316LVM
<i>Cover</i>	3D Tetra4	267,582	0.4 – 0.5	AISI 316LVM
<i>Pin</i>	3D Tetra4	46,147	0.2 – 0.3	AISI 316LVM
<i>Inclined Plane</i>	3D Tetra4	33,209	0.4 – 0.5	AISI 316LVM
<i>Bone</i>	3D Tetra4	230,396	1.8 – 2.2	Sawbones®
<i>Rollers</i>	2D Shell	21,336	0.8 – 1.2	Stainless steel
<i>Screws</i>	1D Beam	4 × 8	/	Stainless steel
Total n° of Elements:		<b>1,148,568</b>		

### 4.2.3 Internal constraint and interactions

Following the physical connections, the main constraints were integrated as represented in *Figure 10*, and described as follow:

- (1) the inclined plane was constrained with the main body, thanks to *1D Beam* and *Kinematic Joints*, that allow the continuity between the master node and the mesh, to represent the screw-drive system (*Figure 10, a*);
- (2) the pin and the main body were constrained with a single axial spring of about 5 N stiffness to simulate the pre-compression between those the Pin surfaces and the wedge-shaped block (*Figure 10, b*);

- (3) the Body and Cover were constrained along their borders with a rigid *Tied constrain*, a master-slave connection between node and elements that reproduce the structural continuity provided by welding (*Figure 10, c*);
- (4) a gap of  $0.1\text{ mm}$  was maintained between the guide and the body along its main borders (*Figure 10, d*), and a gap of  $0.05\text{ mm}$  was maintained between the pin and housing (*Figure 10, e*), according to physical design.

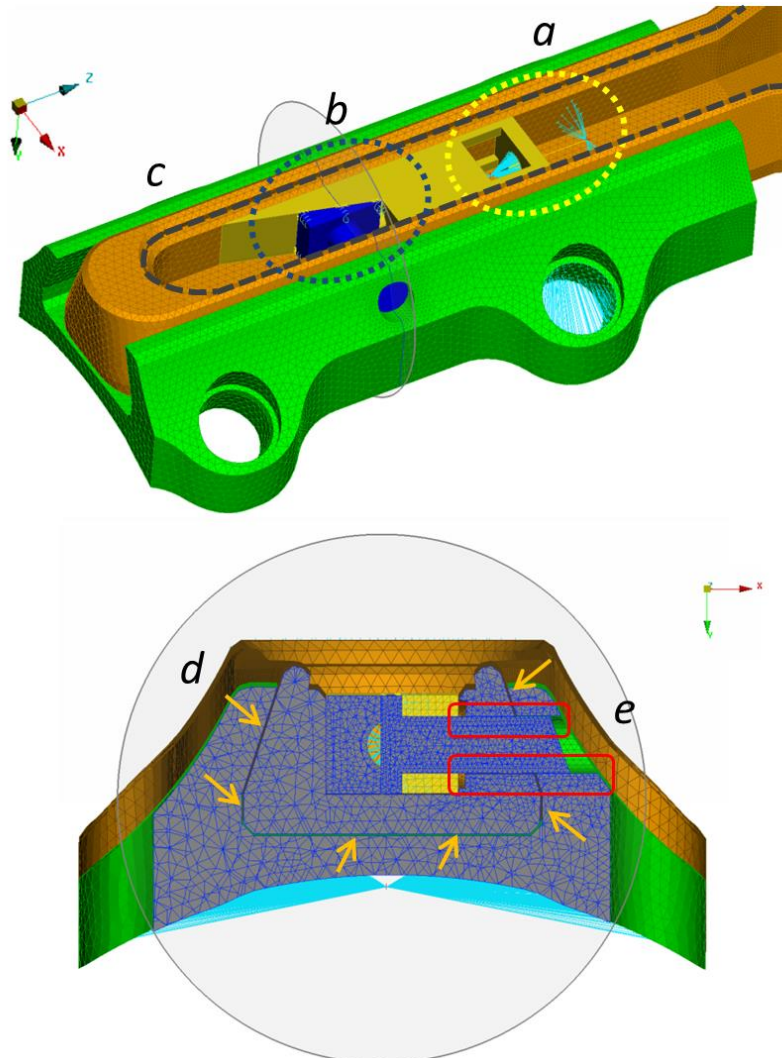


**Figure 9:** Main constraints related to plate internal components (a, b, c) and section detail the mechanical play between the multiple parts (d, e).

#### 4.2.4 Contact description and parameters

The reciprocal interactions between internal parts were modeled with the standard *pressure-overclosure* formulation, using the Soft Contact representation with exponential definition. The simulated parameter range has been highlighted in *Table 6*, and two specific formulations have been defined as detailed in *Table 7*.

**Table 6.** Main parameters to be defined in the model for the standard pressure-overclosure formulation with exponential definition.

Parameter	Range	Model influence
<i>Initial pressure (MPa)</i>	(20, 60)	It indicates the pressure between the two surfaces when the gap registered in the model is equal to the initial gap parameter set into the contact card definition
<i>Initial gap (mm)</i>	(0.05, 0.1)	It indicates the value of the gap at which the pressure between the two surfaces should be equal to the initial pressure parameter set into the contact card definition
<i>Friction coefficient (l)</i>	(0.05, 0.15)	It indicates the value of friction (both static and dynamic) that acts for the calculation of the tangential force between the surfaces in contact

**Table 7.** Detail of the two contact parameters simulated into the FE model.

Name	Values	Involved interaction
<i>“Softer” contact</i>	<ul style="list-style-type: none"> <li>Initial Gap: 0.05 mm</li> <li>Initial Pressure: 20 MPa</li> <li>Friction: 0.05</li> </ul>	Main Body vs. Guide; Bone vs. Main Body; Bone gap vs. Bone gap;
<i>“Harder” contact</i>	<ul style="list-style-type: none"> <li>Initial Gap: 0.05 mm</li> <li>Initial Pressure: 60 MPa</li> <li>Friction: 0.05</li> </ul>	Pin vs. Body-Guide Holes; Wedge-shape block vs. Main Body and Cover; Pin vs. Wedge-shape block;

#### 4.2.5 Simplified setup description

A simpler model has been developed to evaluate a possible simplification of the analysis. In this case, one extremity was fully constrained with a *Rigid body* (MPC), while an opposite reaction of  $29\text{ N}\cdot\text{m}$  was applied at two central points corresponding to the middle central body and guide screws. The only plate was modeled and then constrained without femur and rollers. The flexural moment has been taken from the fatigue limit of a referenced static plate, subjected to a pulsating, constant amplitude load ( $R = 0.1$  with  $R$  being the ratio between the minimum and maximum load), to reproduce the maximum bending moment deriving from the same regulation's *four-point bending* test.



**Figure 10:** The simplified FE model with constraints and loads applied to this specific plate.

### 4.3 Experimental test setup

The *Instron Electropulse E3000* was used for the experimental tests campaign. This axial-torsional machine can deliver up to  $3000\text{ N}$  of axial load and up to  $25\text{ N}\cdot\text{m}$  of torque, with a resolution equal to  $0.001\text{ N}$  and repeatability below  $0.124\%$  for the axial load cell. The testing machine was equipped with the upper grip that bears two rollers, whose distance was set equal to ' $a$ ' ( $83\text{ mm}$ ), and with the lower grip that bears two other supports, whose distance was set to ' $2h + a$ ' ( $237\text{ mm}$ ) according to ASTM F382.17 regulation. Tests were realized in static mode, with a displacement controlled rate equal to  $5\text{ mm}/\text{min}$  in conformity with previous analysis (Terzini et al., 2020). The ASTM F382.17 regulation prescribes a four-point bending test to identify the plate's bending stiffness and bending strength. The unusual shape of the bone plate requires adapting the standard prescriptions to solicit the critical portion of the device. An anatomical replica of the femur (Sawbones®, Europe AB, Malmö, Sweden) has been used as a load application extension to evaluate a more realistic configuration of the bone plate position. Two main conditions were analyzed: the plate was mounted on an integer femur to simulate bone behavior when an 'ideal' healing process has terminated; the plate was mounted on a fractured femur (with a B2 diaphysis fracture from AO/OTA classification) to test the plate flexural stiffness without the bone influence.

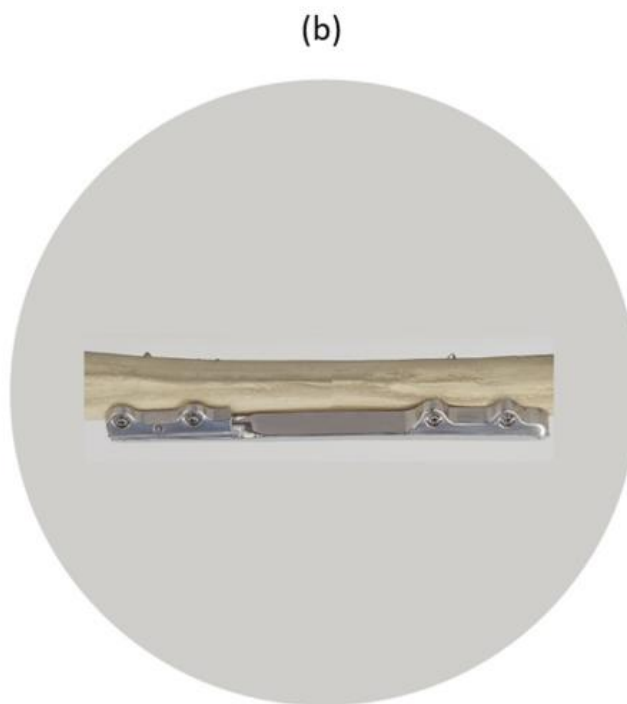
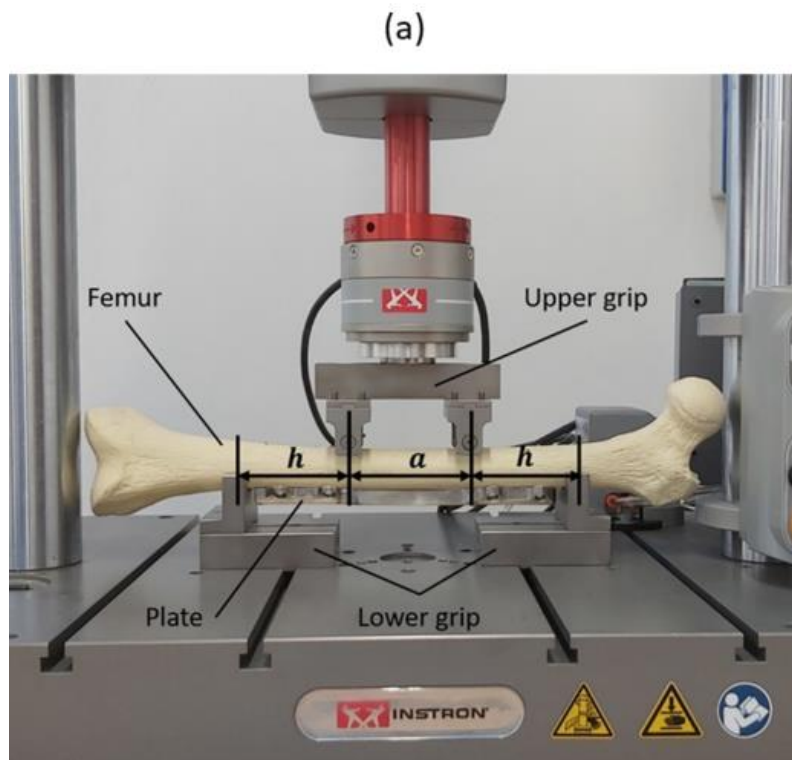


**Figure 11:** Four-point bending test with Instron Electropulse E3000: (a) loading set up; (b) plate detail.

## 4.4 FE model for fracture healing study

The last part focuses on analyzing and investigating the influence of physiologic load conditions on plate stress and inter-fragmentary strains (*IFS*) along the fracture gap. Previous analyses have recommended using diaphysis fracture with an oblique or a more straightforward horizontal shape (32A for *AO/OTA classification, Figure 12*). The difference between the conceived wireless dynamizable plate and some commercial referenced plates has been highlighted.

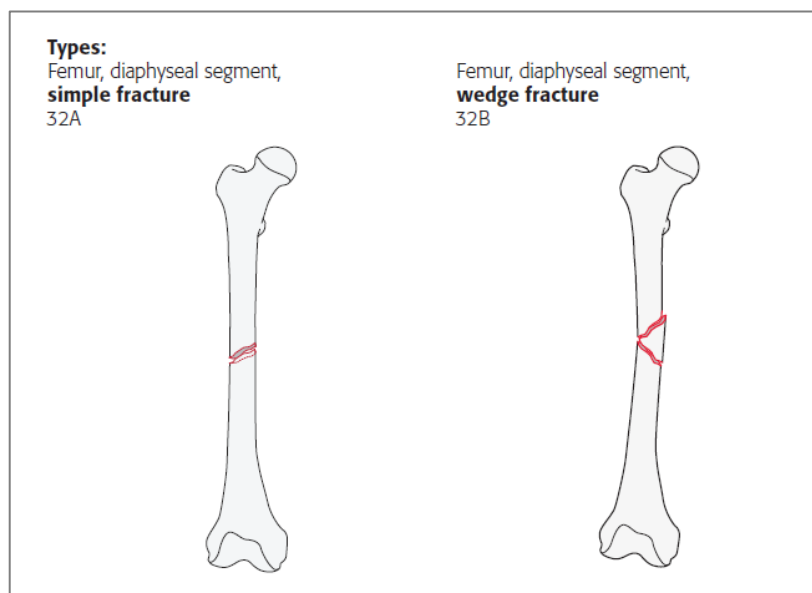


**Figure 12:** Standard of fracture types following the AO/OTA classification.



#### 4.4.1 Building the new FE model

A standard horizontal fracture with a variable gap of 1 to 5 mm has been generated and integrated into the model, and the Elastic modulus of the callus tissue has been selected from the literature, as represented in *Table 8*. The model allows evaluating the influence of the designed plate geometry and screws positioning into the fracture healing process. The plate static strength and the interfragmentary movement (*IFM*) in the first post-operative phase have been evaluated using the model without a continuum between the two pieces of bone.

**Table 8.** Main Elastic Modulus for a referenced fracture healing process.

Tissue analyzed	Young Modulus [MPa]	References
<i>Fibrocartilage</i>	60	<i>Stainer et al., Perren et al.</i>
<i>Immature Callus</i>	120	<i>Stainer et al., Perren et al.</i>
<i>Mature Callus</i>	600	<i>Stainer et al., Perren et al.</i>
<i>Cortical bone</i>	16'000	<i>Stainer et al., Perren et al.</i>

#### 4.4.2 Selecting the worst physiologic load condition

The first step in comparing the structural and biomechanical performances of different internal fixation plates is to select a representative physiological load condition. The first approximation is the Pauwels model, which evaluates the femoral head's contact force and the great trochanter's muscle force, starting from the subject's body weight and respective mechanical arms. The two main

drawbacks of this study are the unstable abductor's muscle and the analysis limited to a 2D projection (Eschweiler et al., 2012). Nonetheless, the force obtained from such approximation is very close to the output analysis of Bergmann and colleagues during the single-leg stance measured on implanted prostheses (Bergmann et al., 2001; Heller et al., 2005) In particular, looking at *Table 9*, the last loading condition has been selected for the study, which considers the action of both *Vastus Femorali* and *Abductor Muscle* forces in a physiologic-like situation in terms of femur sollicitation (Duda et al., 1998; E. F. Rybicki, F. A. Simonen and E. B. Weis, 1972).

**Table 9.** Details of loading conditions were analyzed for the fracture healing studies.

	$\mathbf{F}_r$ [N]			$\mathbf{F}_m$ [N]			
	$ \mathbf{F}_{rx} $	$ \mathbf{F}_{ry} $	$ \mathbf{F}_{rz} $	$ \mathbf{F}_{mx} $	$ \mathbf{F}_{my} $	$ \mathbf{F}_{mz} $	
	668.0	/	1980.4	668.0	/	1144.4	[1]
<b>Pauwels vs. Bergmann</b>	651.0	126.5	1921.0	/	/	/	[2]
	370.8	225.2	1573.9	83.2	127.0	637.9	[3]
<b>Notes:</b>	[1] Pauwels force estimation, with a partial BW of 85 kg						
	[2] Bergmann, with a resultant force of 2032 N on the femoral cup prostheses						
	[3] Bergmann force estimation, with a partial BW of 70 kg						

# **Chapter 5**

## **Results and discussion**

---

This chapter focuses on the FE and MB models' main results and discusses the primary limits considered in the modeling phase.

## 5.1 Multi-body analysis of the un-locking mechanism

The multi-body analysis has been adopted to find the optimal configuration to minimize the actuation system's power and force to disengage the *pin*. The parameters playing a significant role in the designed mechanism are:

- The *friction coefficient* between all interacting parts, i.e., the inclined plane and pin-head, the inclined plane and reciprocal body cavity, the pin, and his housing;
- The *stiffness* and *pre-load* of the spring, which depend on his tiny geometry that is a function of pin dimension;
- The *plane's sliding angle* ( $\Phi$ ) depends on the tiny space available to place the designed unlocking mechanism.

The main outputs of the analysis are reported in *Figure 13*, considering the minimum friction coefficient of the system and the maximum spring stiffness:

- static friction coefficient equal to *0.15*;
- spring stiffness equal to *20 N/mm*;

It is possible to consider the following characteristics related to the mechanical system: the higher the inclination, the smaller the unlocking force, and the higher the locking force; the higher the spring pre-load, the higher the unlocking and locking forces. Overall, minimizing the unlocking power that is the main objective of this analysis would require a higher plane inclination ( $18^\circ$ ) and

a minimum spring pre-load ( $20\text{ N}$ ) to guarantee pin motion, overcoming friction forces between the pin and the respective hole. The required power to unlock the plate equals  $18\text{ mW}$  in the last conditions, while re-locking requires above  $50\text{ mW}$ . Findings have confirmed the relevant role of the friction coefficient on the system performance and revealed a linear ( $R^2 = 0.99$ ) relationship between this coefficient and the maximum required power.

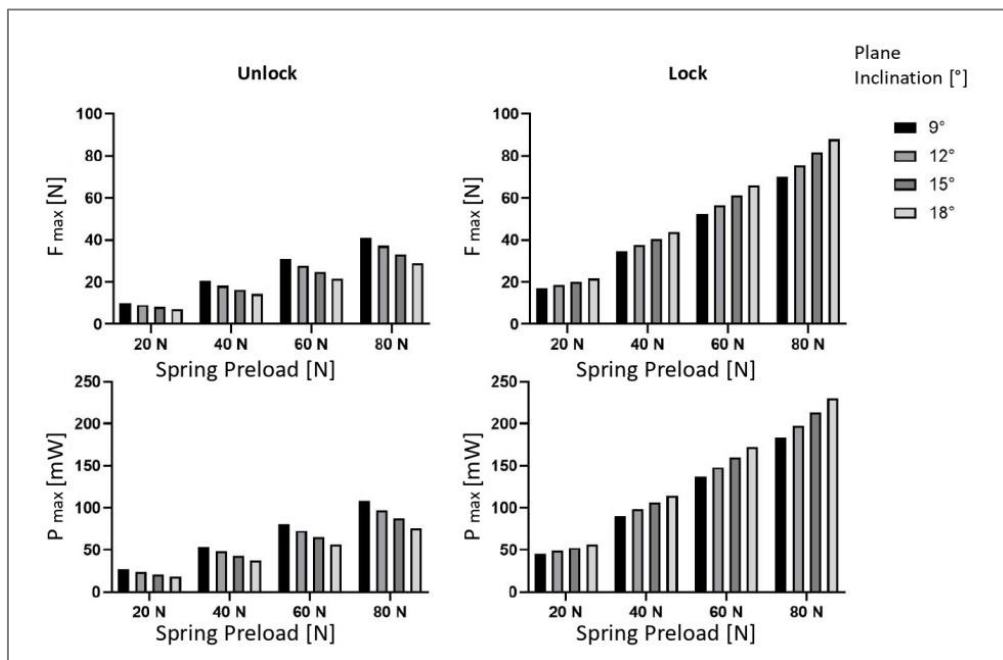


**Figure 13:** Main results of multi-body model (friction coefficient: 0.15, spring stiffness:  $20\text{ N/mm}$ ).

## 5.2 FE analysis of the certification tests

The ASTM F382-17 regulation focuses on the “Standard Specification and Test Method for Metallic Bone Plate.” It describes the precise testing condition and the main physical characteristics needed to obtain the CE signature, considering a metallic bone plate (ASTM International, 2008).

### 5.2.1 Evaluation of plate fatigue limit

According to the producer's data, the stress amplitude limit of the constitutive plate material equals  $400\text{ MPa}$  for  $R = -1$  (fully reversed loading), while  $920\text{ MPa}$  is the ultimate load  $800\text{ MPa}$  as yield stress (SA., n.d.). The fatigue test evaluation with an R factor equal to  $0.1$  corresponds to  $187\text{ MPa}$  of average stress and  $153\text{ MPa}$  of stress amplitude (Robert C. Juvinall, 2012). Regarding the simplified setup, the simulation results show that the *peak von Mises stress* equals  $340\text{ MPa}$ , and it is reached in a tiny portion of the main plate body (*Figure 14*). In addition, a very unfavorable estimation is being performed because the peak load is reached in a very localized area at a taper of the main body section; as such, it would result in local plasticization, which finally would provide residual stress opposite to the applied stress (considering that fatigue stress is performed with pulsating stress, as required by orthopedic plate certification). Consequently, the stress amplitude limit according to fatigue strength calculated by the Haigh diagram with  $R = 0.1$  would result in  $261\text{ MPa}$  (*Figure 15*). At the same time, the

plate's safety factor equals  $1.71$ , which is an acceptable value according to ASTM F382-17 regulation criteria (ASTM International, 2008).

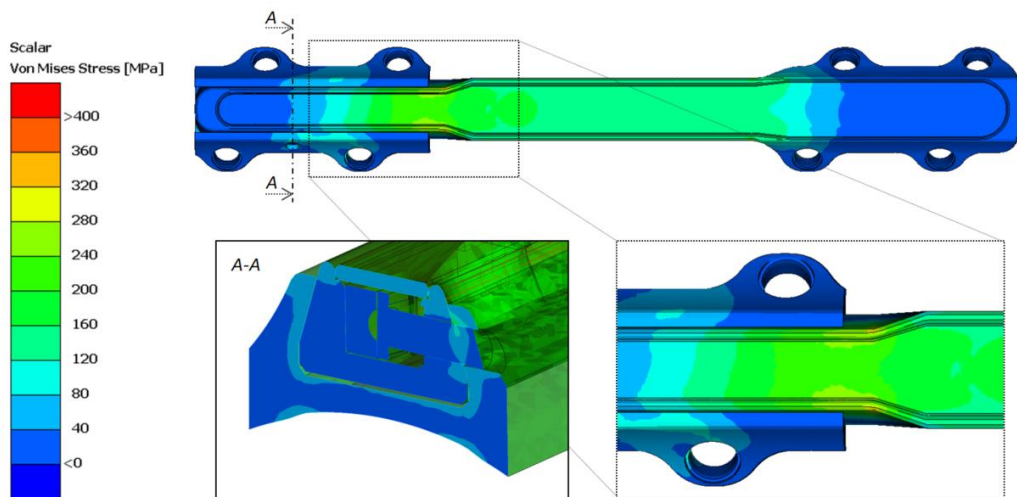


**Figure 14:** Maximum von Mises stress at fatigue bending limit of  $29\text{ N}\cdot\text{m}$ ; detail pin section (A-A) and plate body shrinkage.

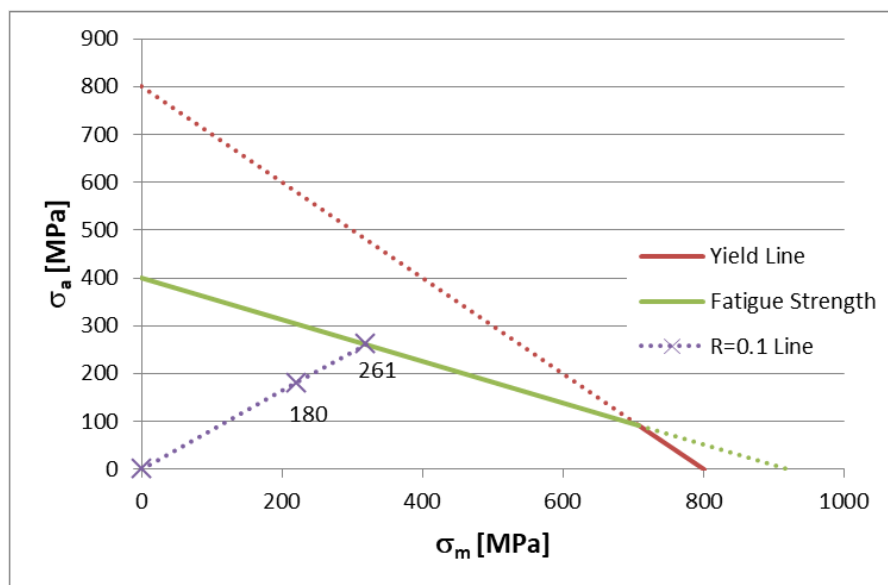


**Figure 15:** Haigh diagram at fatigue bending limit of  $29\text{ N}\cdot\text{m}$ , obtained with  $R=0.1$  factor and a stress amplitude limit of  $400\text{ MPa}$ .

### 5.2.2 Evaluation of static structural strength

The whole setup that applies the maximum static load of  $2\text{ kN}$ , the most stressed point, remains in a precise portion of the plate's main body, with a von Mises stress of  $923\text{ MPa}$  (*Figure 16*). It should be noted how the maximum bending moment from experimental tests has been equal to  $75.3\text{ N}\cdot\text{m}$  (obtained by multiplying half load,  $978.5\text{ N}$  by its arm equal to  $77\text{ mm}$ ). This result is beyond  $29\text{ N}\cdot\text{m}$  applied in the finite element model to compare results to others obtained for a similar non-dynamizable plate. Also, even  $75.3\text{ N}\cdot\text{m}$  did not produce a plate's failure or any of its components in static experimental tests, confirming numerical FE analysis findings. Besides that, at *33% of the maximum load*, which would correspond to a bending moment equal to  $25.3\text{ N}\cdot\text{m}$ , the peak stress is equal to  $299\text{ MPa}$  (*Figure 17*), confirming a good approximation of the simplified setup adopted for the fatigue strength evaluation.



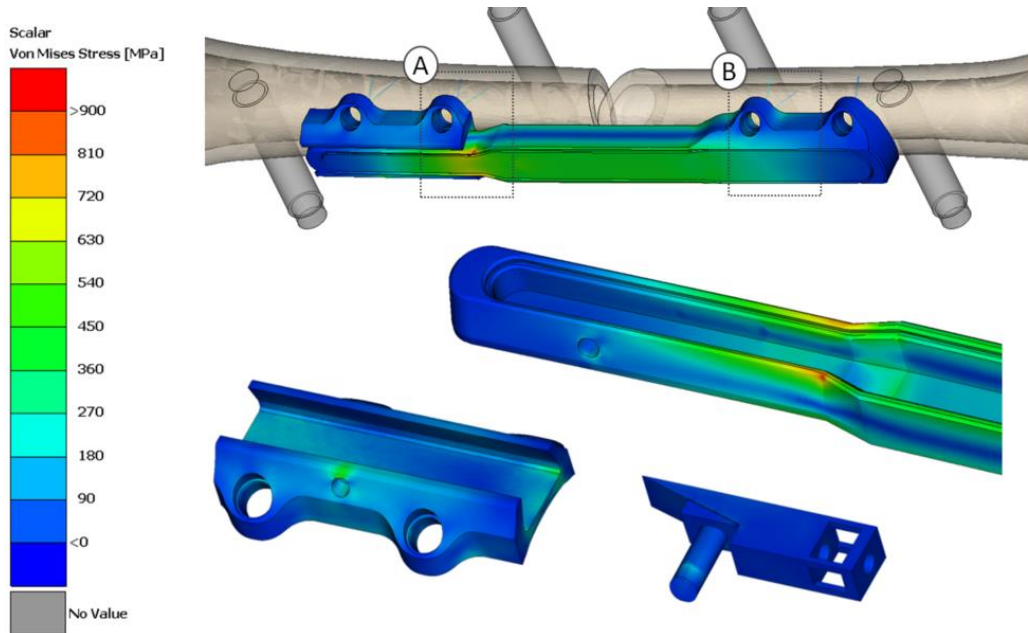


**Figure 16:** Maximum von Mises stress [MPa], at peak static load of 2 kN; detail of the entire plate components and the most stressed screws.

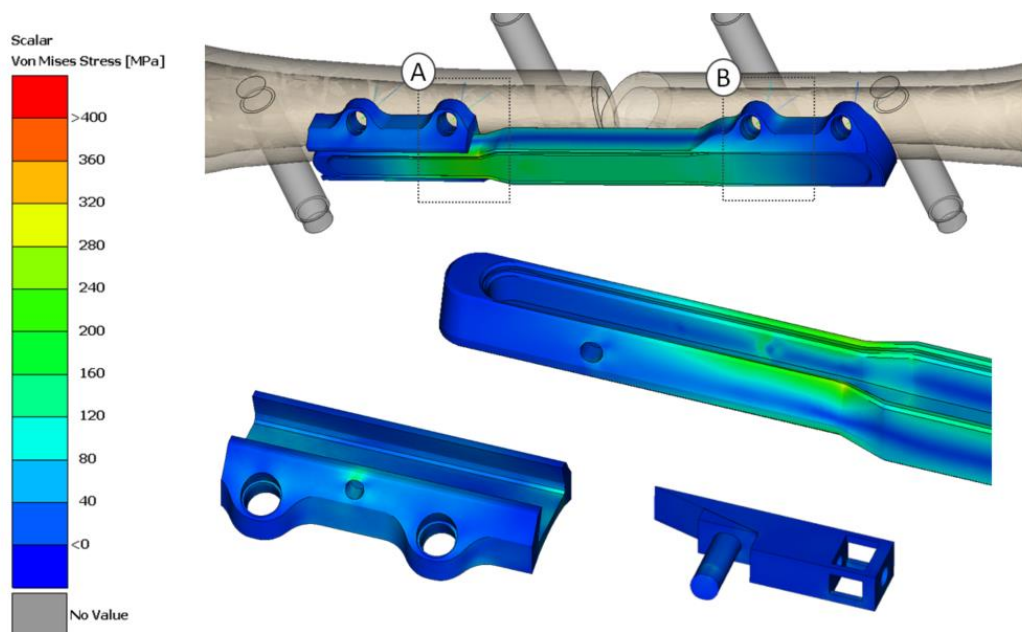


**Figure 17:** Maximum von Mises stress [MPa], at 33% of experimental peak static load: 660 N; detail of the principal plate components and the most stressed screws (A and B boxes).

### 5.2.3 Evaluation of the maximum pressure contact

The plate's maximum contact pressure is localized at the pin's most stressed area, equal to  $376 \text{ MPa}$  (Figure 18). This value depends on the interaction adopted to evaluate the contact between the modeled surfaces, as detailed in the contact definition.

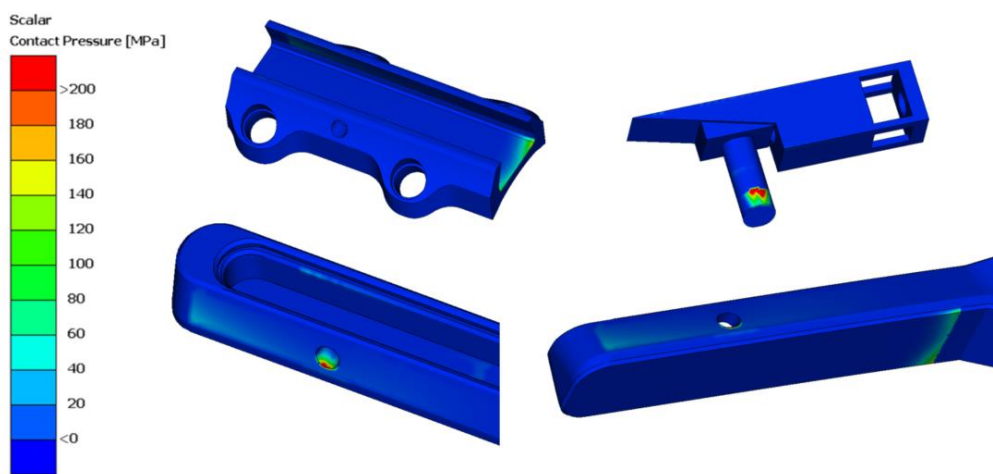


**Figure 18:** Maximum contact pressure [MPa] at the peak static load of  $2 \text{ kN}$  with detail of structural plate components.

### 5.3 Experimental results

According to regulation, the flexural stiffness was calculated from the force-displacement curve's linear slope, while output data were checked with a referenced static device, whose stiffness is equal to  $253\text{ N/mm}$  and whose bending moment at failure is equal to  $29\text{ kN}\cdot\text{mm}$  (Terzini et al., 2020). According to experimental tests, the integer sample sustained the load up to  $2000\text{ N}$  without damage (the test stopped at  $2000\text{ N}$  to prevent prototype failures), while the fractured one failed at  $1957\text{ N}$ . The plate remained intact, but the bone broke, with a second fracture which was indeed visible in the proximity of the right lower support. Considering this second result, comparable to an ASTM F382 standard four-point bending test, the peak load was  $18\%$  lower than  $2400\text{ N}$ , measured for the static reference plate. However, it was estimated to be satisfactory, considering other orthopedic plates' performance on the market (Terzini et al., 2020). As a consequence of the healing process, the bone/plate system's secant stiffness can improve up to  $20.2\%$ . The same experimental tests allowed us to calculate this plate's bending stiffness, equal to  $370\text{ N/mm}$ , which is  $+46\%$  compared to the static reference plate. An experimental error could not be evaluated since one specimen was considered; however, similar tests on the reference plate resulted in a  $5\%$  variability.

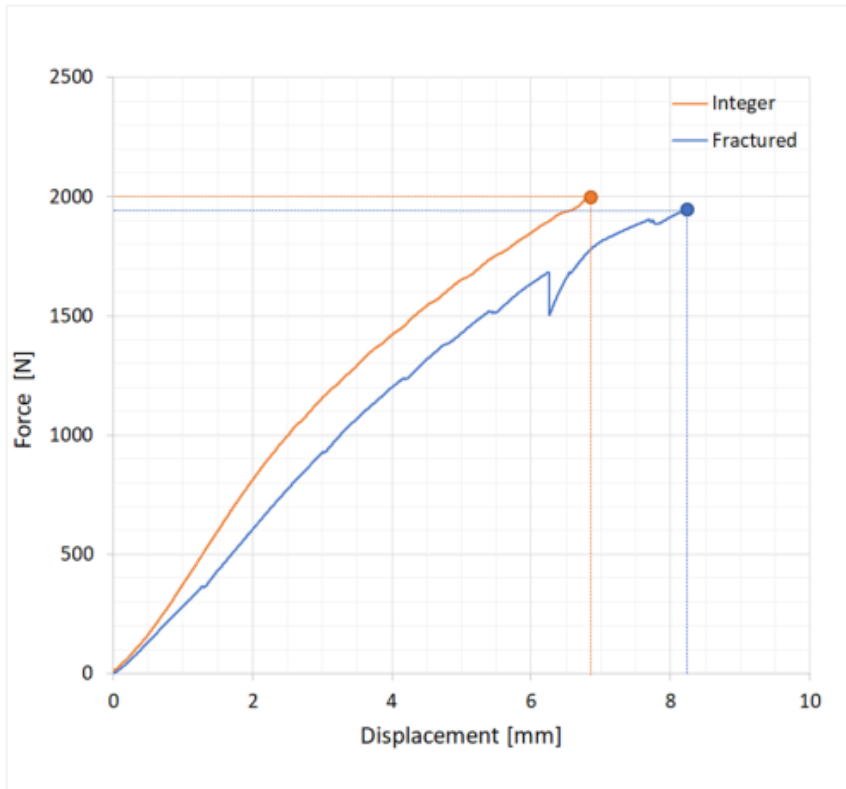


**Figure 19:** Force-displacement curves obtained from the experimental tests for integer and fractured samples: the red arrow marks the point where the femur broke.

## **5.4 FE analysis of the fracture healing process**

The fracture healing study and evaluation of the dynamization performance are based on extensive knowledge that combines numerical and experimental methods with biological and biomechanical findings (Einhorn & Gerstenfeld, 2015; Ghiasi et al., 2017; Glatt et al., 2017). Despite this, numerical FE analysis can be a fundamental step in analyzing the physiologic influence of different load conditions on fracture healing parameters (i.e., *IFS* and *IFM*) and comparing the performances obtained by different types of plates.

### **5.4.1 Main results of the horizontal fracture**

This chapter has analyzed the differences between a traditional referenced static femoral plate and the here projected dynamic plate (both in the locked and unlocked configuration) in terms of stress and strain of the callus tissue (Steiner et al., 2013, 2014b). A local cylindrical coordinate system has been created for each callus volume to evaluate the three principal stress and strain for axial and transversal components. The nine-element matrix has been obtained for each combination of parameters to highlight quantity variations over the entire callus volume. An example of the model has been shown in *Figure 20* to show the bone callus orientation concerning the plate position. The quantities of interest have been evaluated for an increasing callus elastic modulus according to a specific

referenced study (Steiner et al., 2014b) and increased fracture gaps (from 1 to 5 mm) both for horizontal and oblique fractures (the standard 32A for AO/OTA classification).

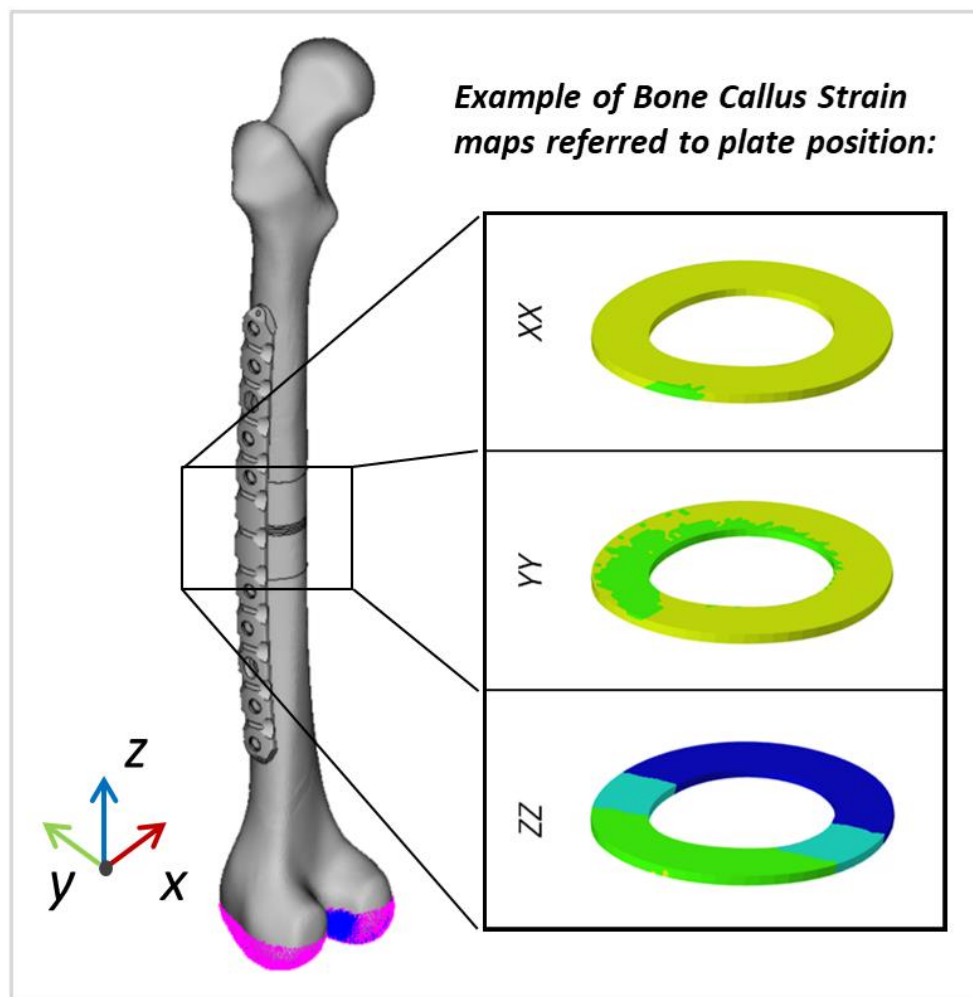


**Figure 20:** Example of bone callus representation concerning the plate position into the complete model. The main axes of the Local Cylindrical-coordinate correspond to the absolute coordinate represented in the Figure.

### 5.3.1.1 Logarithmic Strain results (/)

The *Logarithmic Strain* (or *True Strain*) is a not-dimensional number that can be expressed as a percentage and tells us the amount of physical deformation corrected by the body volume variations. It comes from the formula, where  $\varepsilon_e$  represent the measured engineering strain:

$$\varepsilon_t = \ln(1 + \varepsilon_e) \quad (3)$$

This quantity has been evaluated for the *Traditional Static Plate* and the *Wireless Dynamic Plate* in the *Locked* and *Unlocked* conditions. The values are divided into three ranges of stimulation according to *Table 10*.

**Table 10.** Classification of IFS axial and shear ranges according to literature.

<b>Tissue analyzed</b>	<b>Axial [%]</b>	<b>Tangential [%]</b>	<b>References</b>
<i>Optimal</i>	( $\pm 2, \pm 10$ )	( $0, \pm 5$ )	<i>Steiner et al., Perren et al.</i>
<i>Acceptable</i>	( $\pm 10, \pm 15$ )	( $\pm 5, \pm 15$ )	<i>Steiner et al., Perren et al.</i>
<i>Unacceptable</i>	( $\pm 15, \pm \infty$ )	( $\pm 15, \pm \infty$ )	<i>Steiner et al., Perren et al.</i>

In particular, it is possible to see how the dynamic plate realizes a better loading condition for the callus tissue, reducing the maximum compression on the opposite side and improving the traction in the proximal district, which should be beneficial for callus stimulation (*Figure 21*). Oppositely, there are no apparent differences concerning the tangential components between the analyzed solution (*Figure 22*).

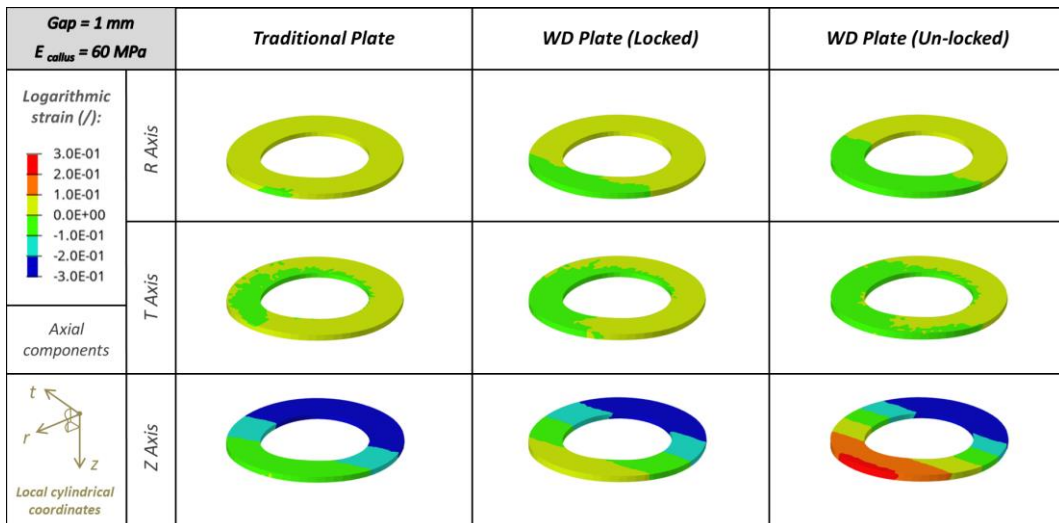


**Figure 21:** Logarithmic Strain contour maps for 1 mm of fractured gap and 60 MPa of callus tissue Elastic Modulus. Focus on the three main *axial components* in a Local Cylindrical System (LCS).

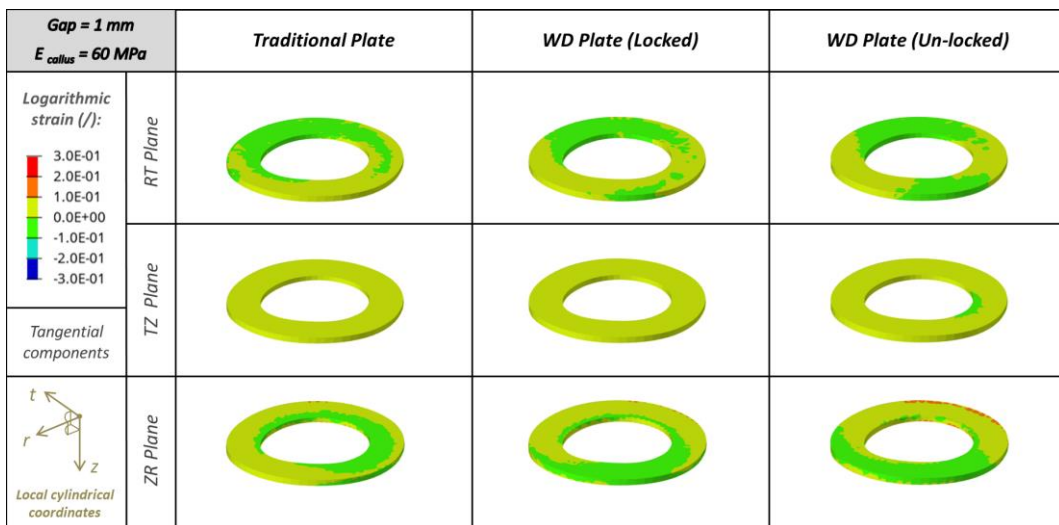


**Figure 22:** Logarithmic Strain contour maps for 1 mm of fractured gap and 60 MPa of callus tissue Elastic Modulus; focus on the three main *tangential components* in a local cylindrical system (LCS).



### 5.3.1.2 Global Stress results (MPa)

Global stress is a dimensional number (usually expressed in MPa) that indicates the body's physical stress at one specific point and can be evaluated concerning the three principal axes of analysis.

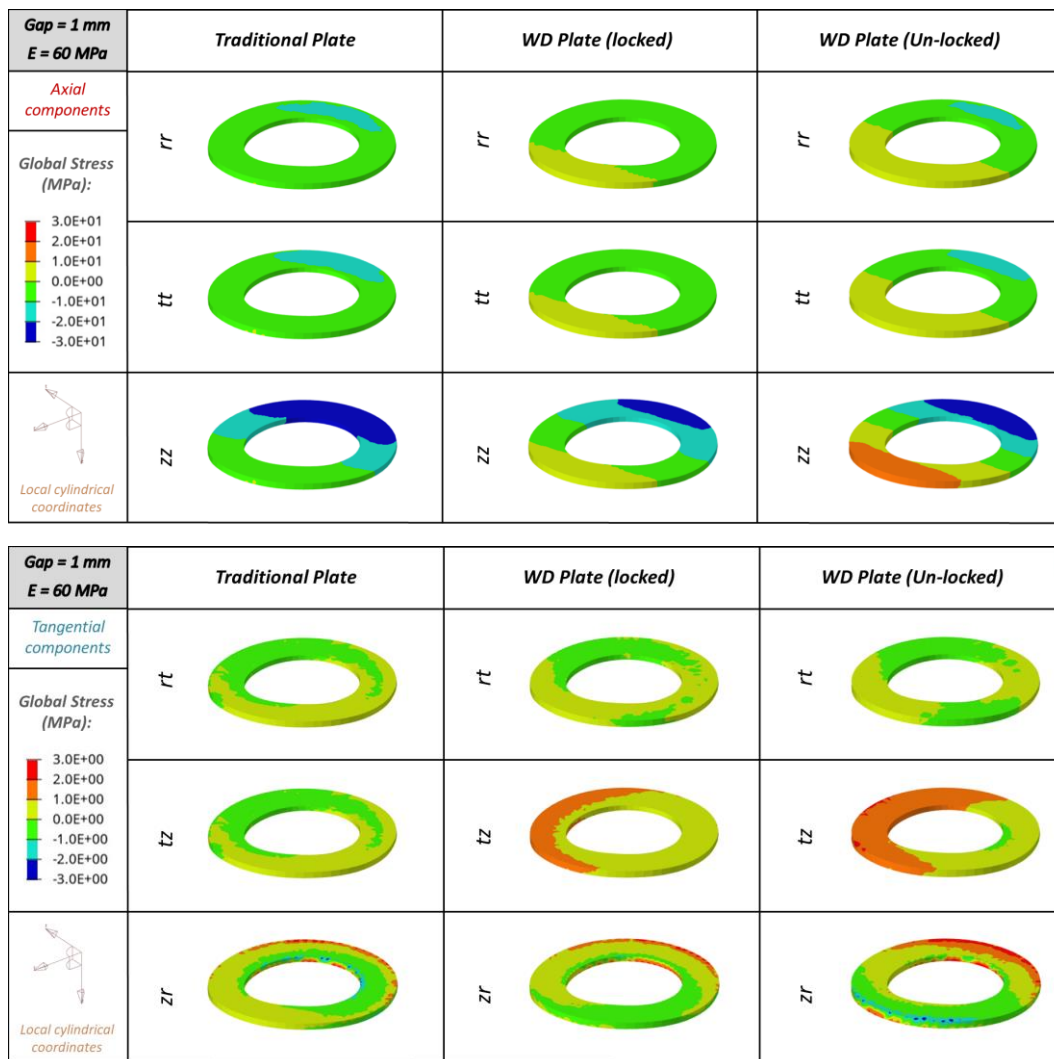


**Figure 23:** Global Stress contour maps for 1 mm of fractured gap and 60 MPa of callus tissue Elastic Modulus; focus on the three main axial and tangential components in a local cylindrical system (LCS).

In this case, looking at *Figure 22*, the Global stress indicates that, for an Elastic Modulus of 60 MPa, the main difference between the Traditional Plate and the Dynamic Plate is the presence of a traction area close to the plate contact area due to the different plate geometry; this traction becomes more significant in the unlocked situation, as highlighted in the *ZZ* component (*Figure 22*). Another phenomenon is visible looking at the *TT* and *RR* components, which show a change in sign, close to the area where the axial stress becomes positive, which indicates that the planar forces are also changing the verses (*Figure 22*). The tangential components can highlight a difference between the *TZ* component, representing one of the tangential forces acting on the callus (*Figure 23*). The more considerable rigidity of the plate to flexural bending for the analyzed situation of 60 MPa can cause tangential stresses on the callus, which may not benefit the initial callus healing process in case of a small fractured gap (L. E. Claes & Meyers, 2020).

## **5.4.2 Analysis of different fracture gap**

Results are primarily confirmed in the incremented fracture gap (3 and 5 mm), with some difference for the tangential global stress results.

### **5.3.2.1 Logarithmic Strain results (/)**

For increased fracture gap, both axial and tangential components show a better situation for Dynamic Plate than the Traditional Plate (*Figure 24-25*).

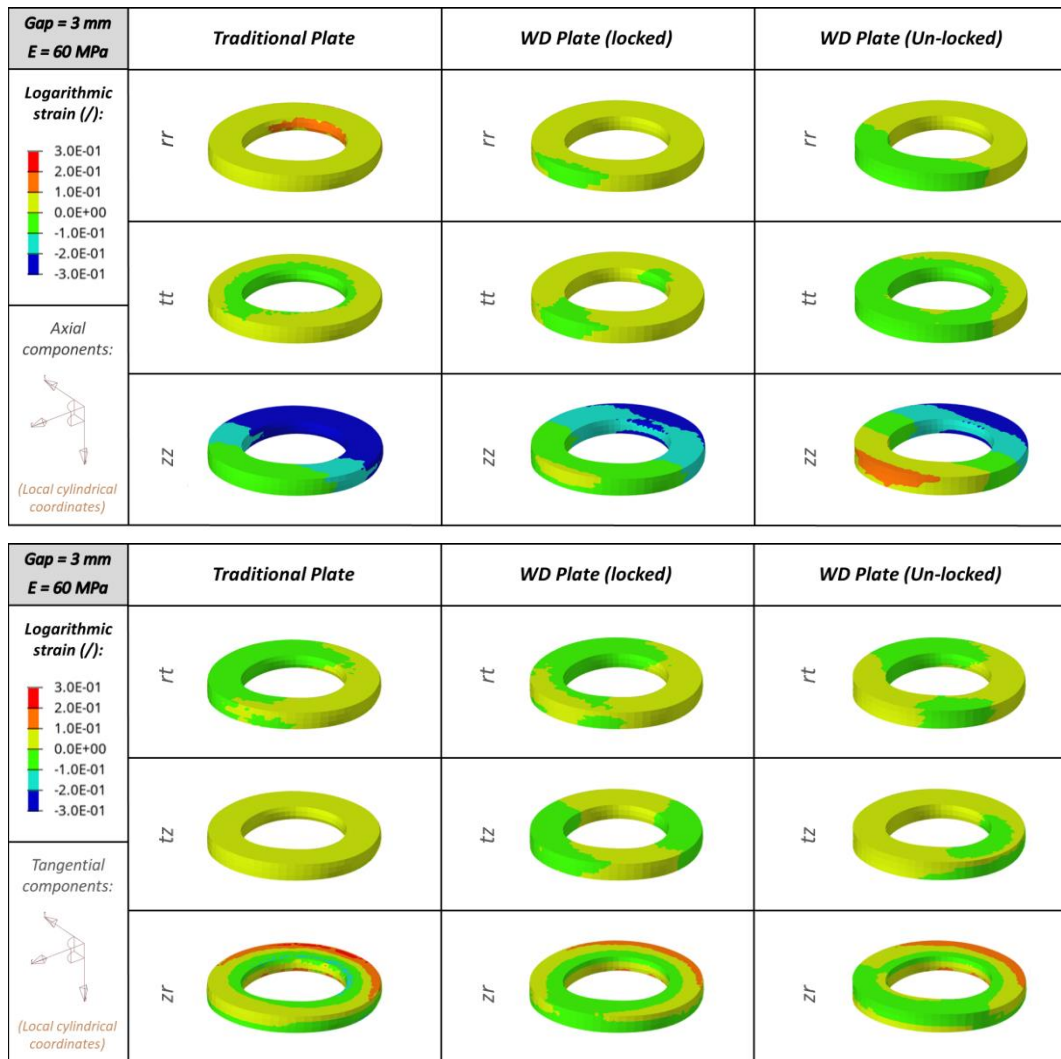


**Figure 24:** Logarithmic Strain maps for 3 mm of fractured gap and 60 MPa of callus tissue's Elastic Modulus. Focus on three main *axial and tangential components* in local cylindrical coordinates.

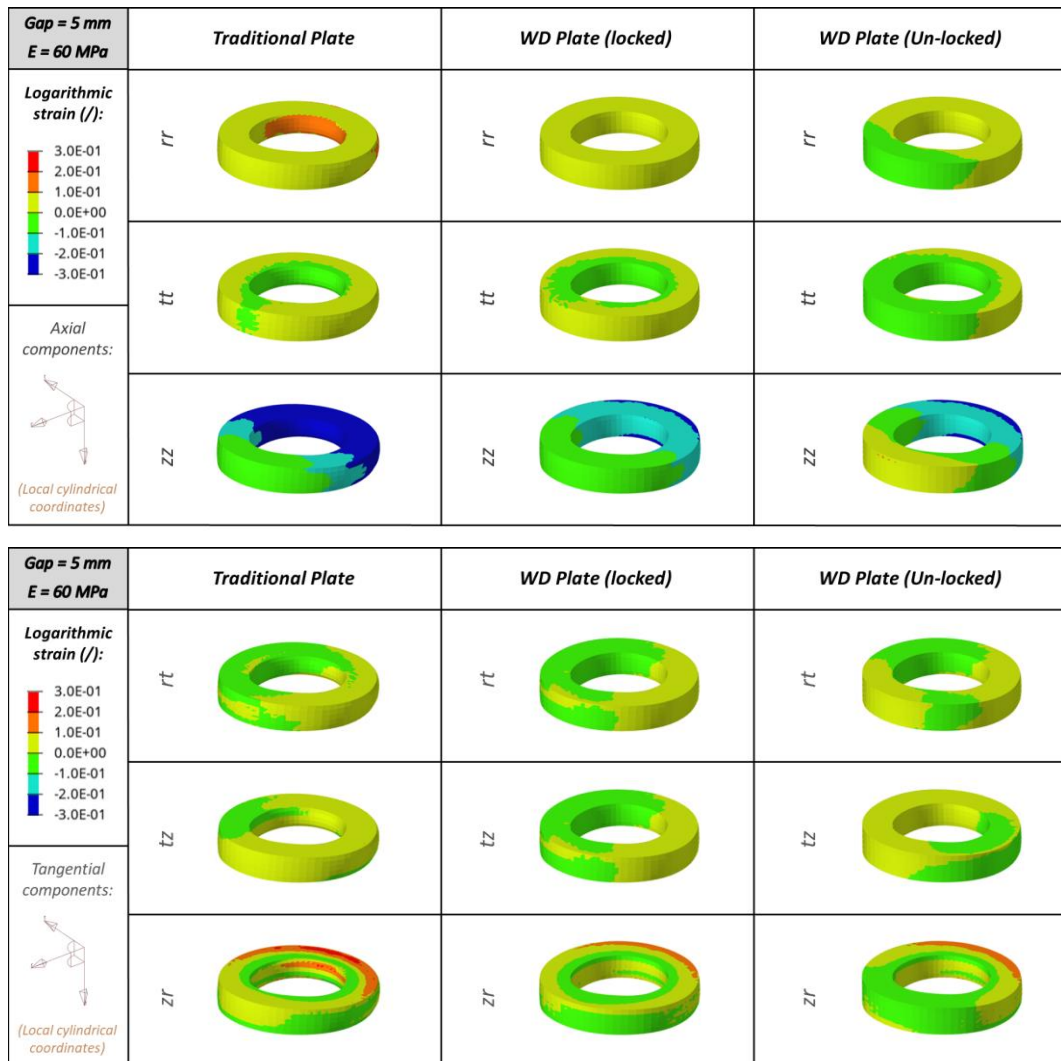


**Figure 25:** Logarithmic Strain maps for 5 mm of fractured gap and 60 MPa of callus tissue's Elastic Modulus. Focus on three main axial and transversal components in local cylindrical coordinates.

### 5.3.2.2 Global Stress results (/)

Looking at the Global Stress of increased fracture gaps, the results evidence that the Dynamic Plate guaranteed the reduction of the compressive stress on the callus and a better distribution of the two tangential stresses (Figure 26-27).

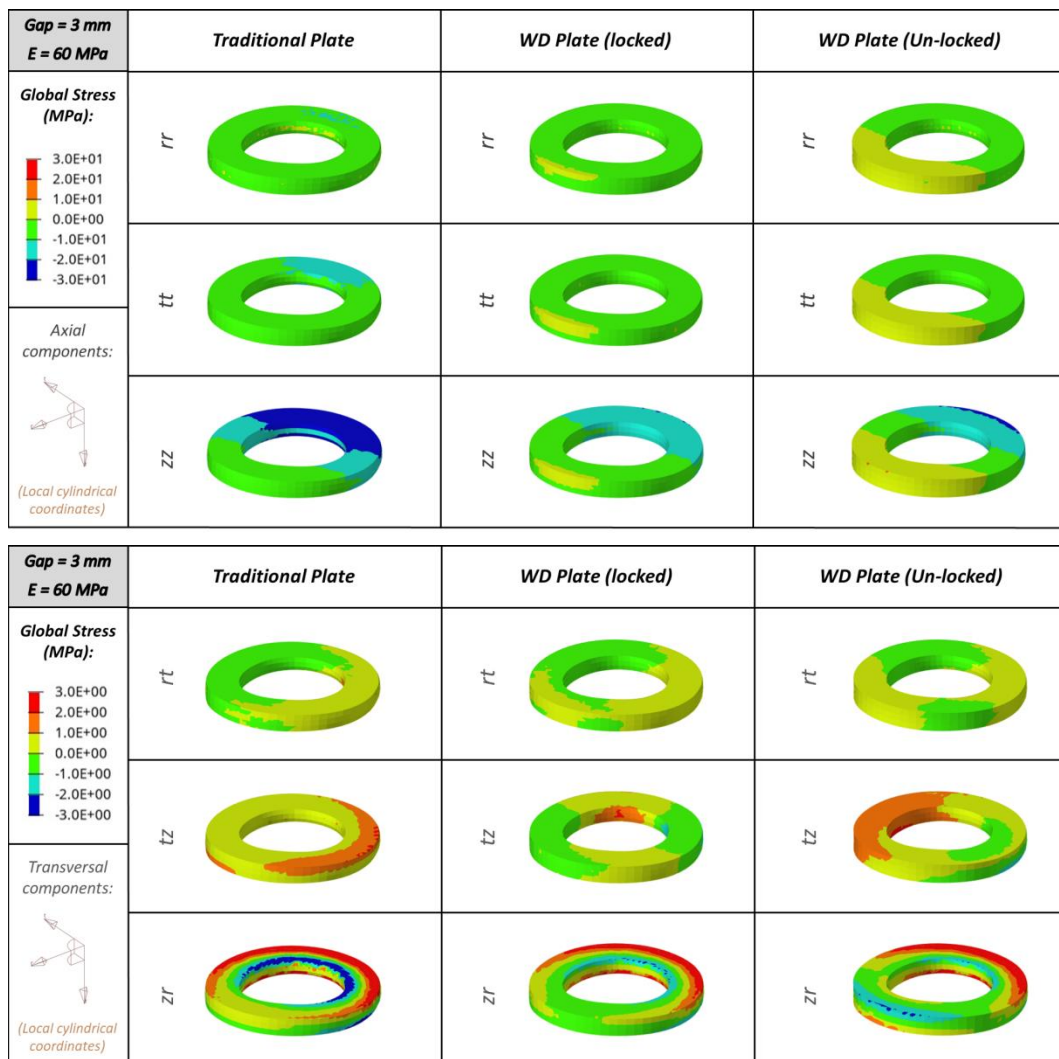


**Figure 26:** Global Stress maps for 3 mm of fractured gap and 60 MPa of callus tissue's Elastic Modulus. Focus on three main axial and transversal components in local cylindrical coordinates.

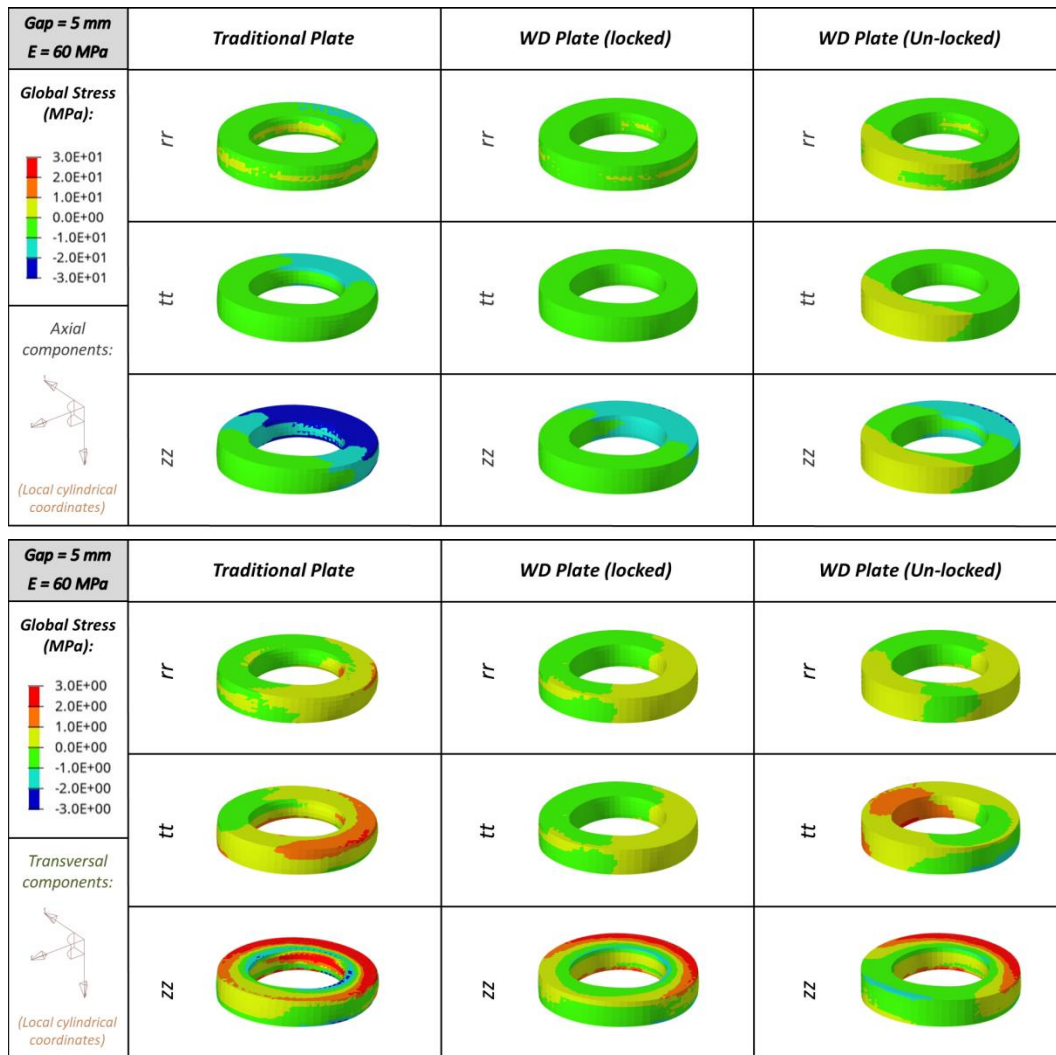


**Figure 27:** Global Stress maps for 5 mm of fractured gap and 60 MPa of callus tissue's Elastic Modulus. Focus on three main axial and tangential components in local cylindrical coordinates.

### 5.4.3 Analysis of different elastic modulus

This section analyzes different *Elastic Moduli* (Steiner et al., 2013, 2014a) of callus tissue to check the advisable time to unlock the plate. The axial and

tangential components have been obtained in the three specific situations for a fractured gap of  $1\text{ mm}$  in a Global coordinate system.

### 5.4.3.1 Logarithmic Strain results (/)

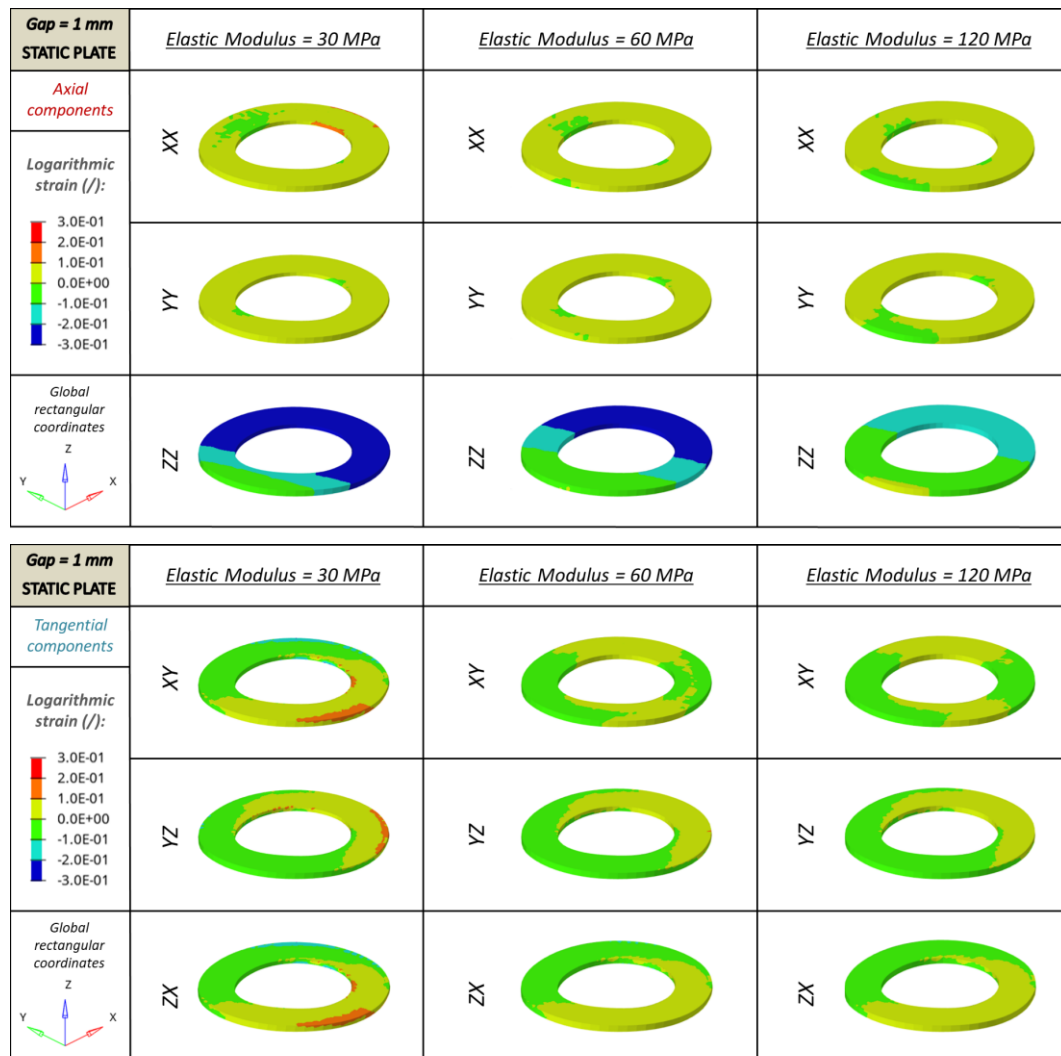


**Figure 28:** Logarithmic Strain contour map for  $1\text{ mm}$  of fractured gap and an increased callus tissue's Elastic Modulus. Focus on the three main *axial* and *tangential* components in local cylindrical coordinates for the *Traditional Static Plate*.



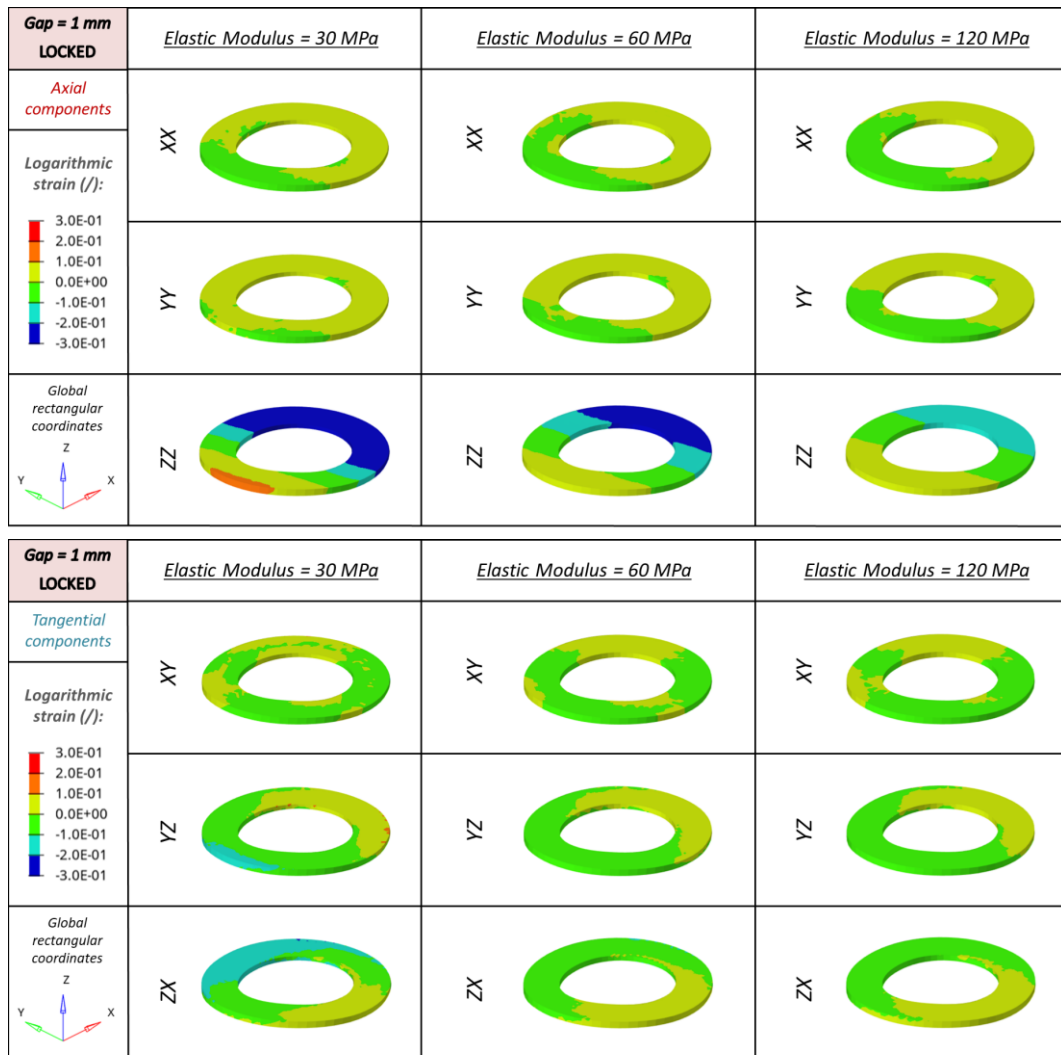


**Figure 29:** Logarithmic Strain contour map for 1 mm of fractured gap and increased callus tissue's Elastic Modulus. Focus on the three main *axial* and *tangential* components in local cylindrical coordinates for the *Dynamic Plate* in the *Locked* configuration.



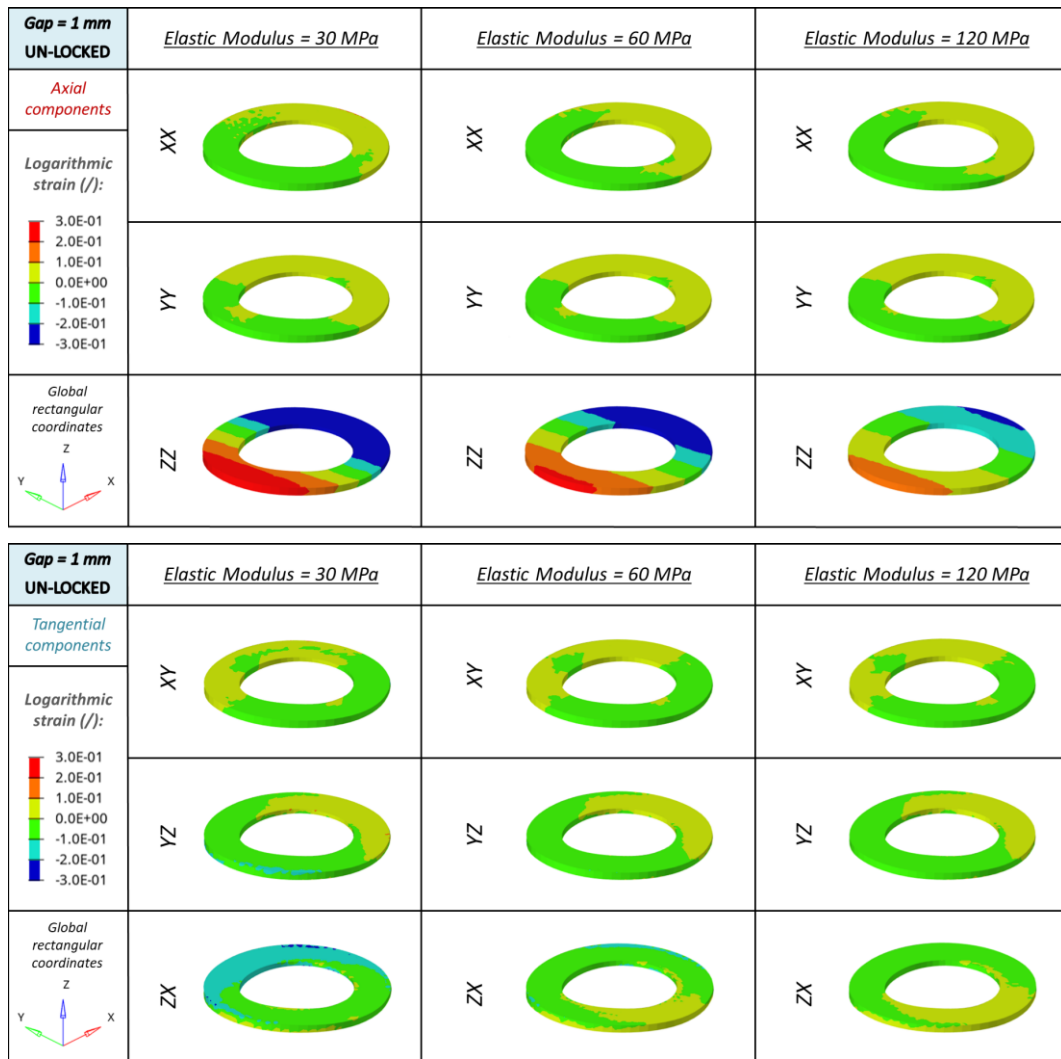


**Figure 30:** Logarithmic Strain contour map for 1 mm of fractured gap and increased callus tissue's Elastic Modulus. Focus on the three main *axial and tangential components* in local cylindrical coordinates for the *Dynamic Plate* in the *un-locked configuration*.

#### **5.4.4 Analysis of minimum and maximum values of IFS**

To look at the previous results from a different perspective, we focus on the *minimum* and *maximum values* of IFS over the entire callus tissue.

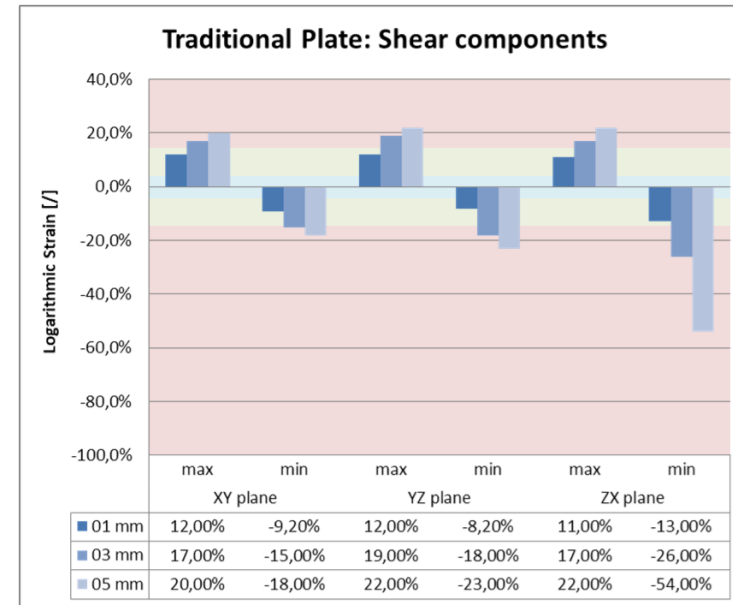
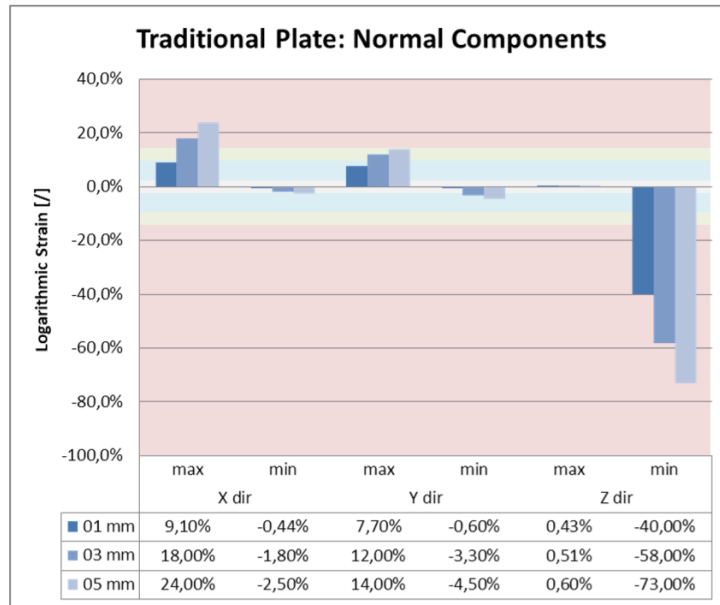
##### **5.4.4.1 Logarithmic strain for different fracture thicknesses (60 MPa)**

The Traditional Static Plate seems to lose its effectiveness for increased fractured gaps, as highlighted in *Figure 31*. The range of *IFS* became critical for the *axial Z* component and *tangential ZX* component: the first grows in negative terms from 40 to 73 % on the femur medial side, while the second grows from 13 to 54 % considering the *negative direction*. The range of IFS in the remaining four components is acceptable both for positive and negative terms and becomes unacceptable only for the tangential terms in the higher fracture gap (5 mm). The Wireless Dynamic Plate shows a better situation, improving his efficacy for increased fracture gaps. The result appears clear both for the *Locked* and *Unlocked* configurations, as highlighted in *Figure 32-33*. For the *axial Z* component, *IFS* values decreased from 33 to 23 % in the locked case and 42 to 33 % in the unlocked one. Other components are in the acceptable zone, which means a good stimulation of the callus tissue for the increased fractured gaps.

##### **5.4.4.2 Logarithmic strain for increasing Elastic Modules (1 mm Gap)**

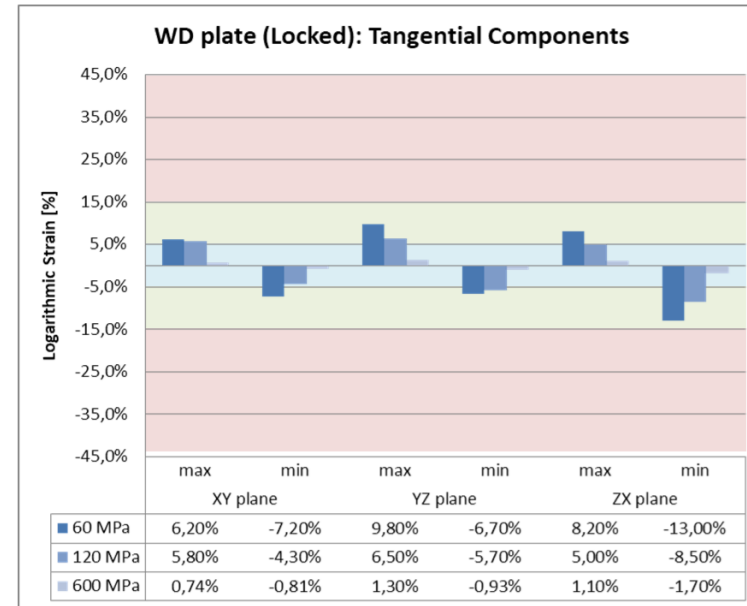
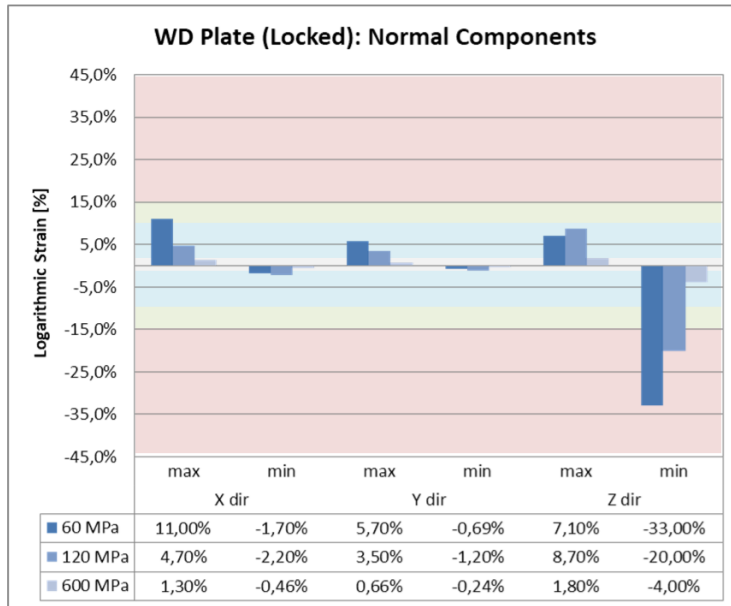
The situation described before is different when looking at the minimum fracture thickness and focusing on increased Elastic Modules (60 to 600 MPa).

The Traditional Static Plate shows the *Z-axis* component to reach a negative value of 40 % for what concern a 60 MPa of callus tissue's Elasticity Modulus (*Figure 34*), while the same *Z axial* component of the Wireless Dynamic Plate reaches a negative value of 33 % in the Locked configuration and 42 % in the Un-locked one. However, Wireless Dynamic Plate slightly improves the stimulation because the lower absolute values of the negative terms are also compensated with a slightly positive value of the same *Z-axis component*, which means a more symmetrical callus stimulation (*Figure 35-36*). Furthermore, the unacceptable IFS values for both the 60 and 120 MPa conditions can be considered clinically safe for the *Traditional Static Plate* and consequently translated to the Wireless Dynamic Plate, which has better results in terms of callus stimulation. To conclude is not clear from this analysis the right moment to un-lock the Wireless Plate, but it seems clear that this operation should be done after callus maturation, i.e., for values of Elasticity more prominent than the considered 120 MPa.



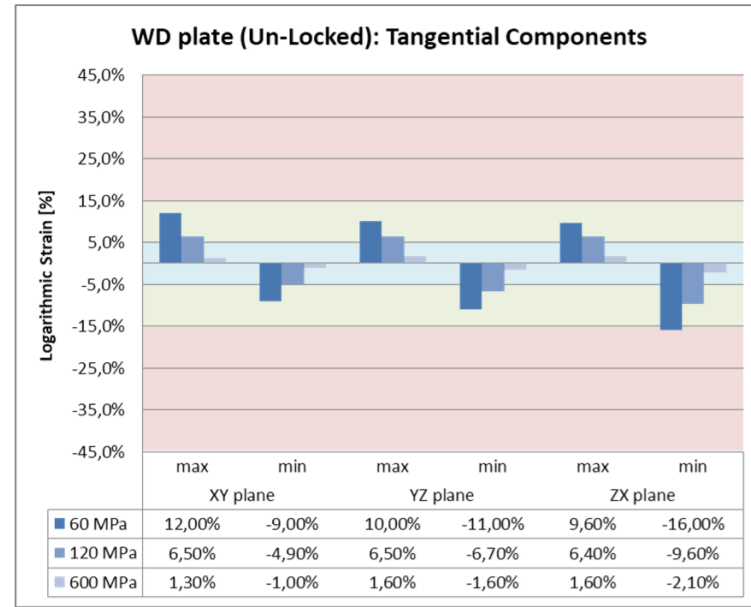
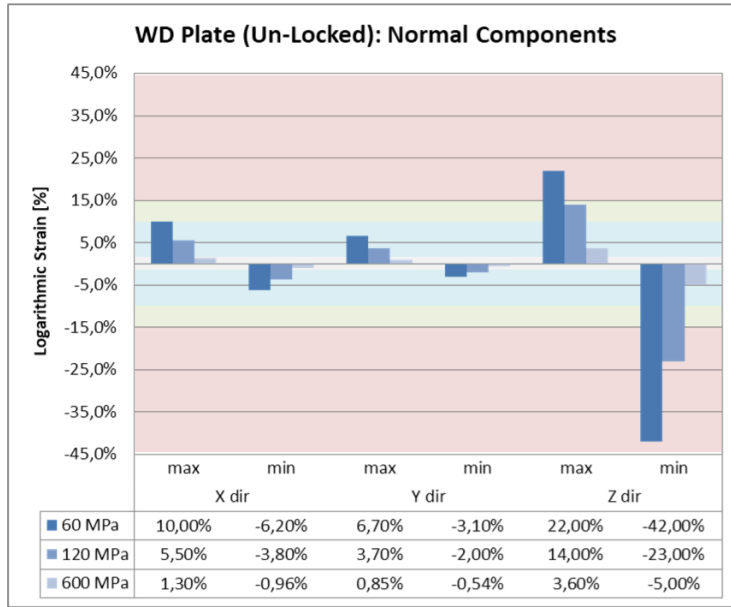
**Range of IFS:**   **Optimal**   **Acceptable**   **Unacceptable**

**Figure 31:** Logarithmic Strain's *maximum* and *minimum* values for the *Traditional Static Plate*. Focus on the three main *axial* and *tangential* components in a global coordinates system for an increased fracture gap (1 to 5 mm) and a fixed Elastic Modulus of 60 MPa.



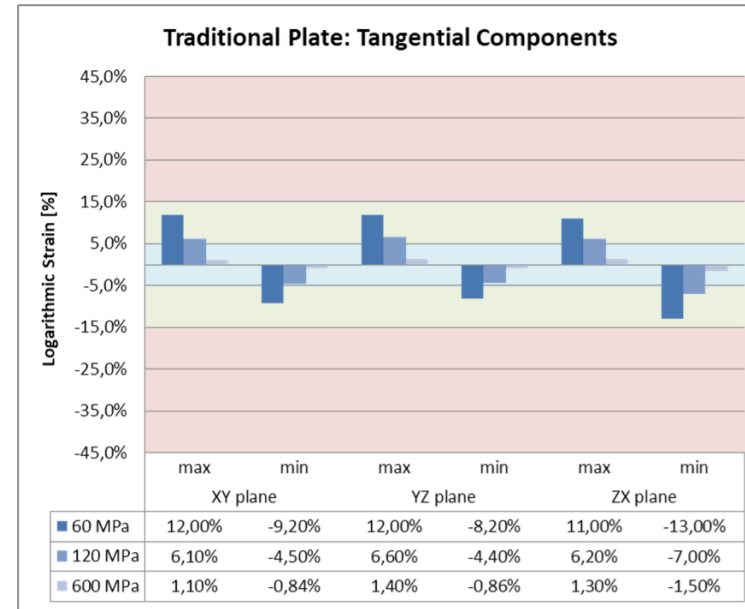
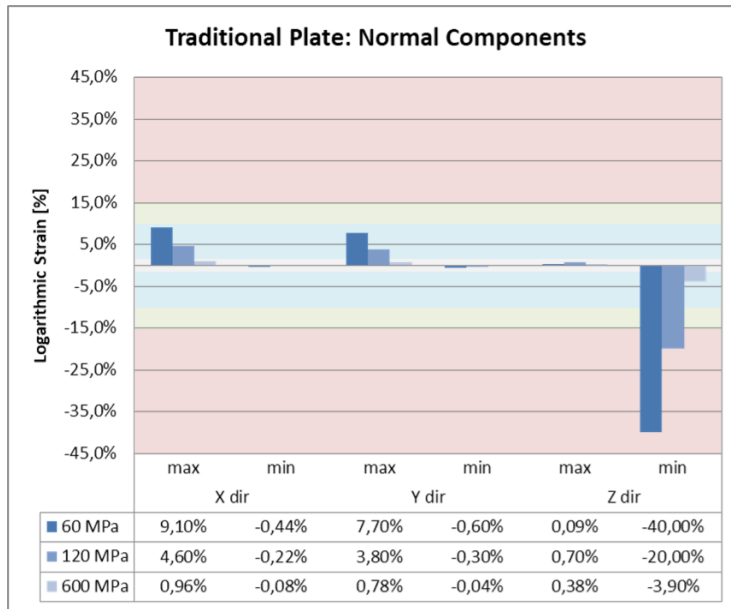
**Range of IFS:** 
**Optimal** 
**Acceptable** 
**Unacceptable**

**Figure 32:** Logarithmic Strain's *maximum* and *minimum* values for the *Wireless Dynamic Plate* in a *Locked* configuration. Focus on the three main *axial* and *tangential* components in a global coordinates system for an increased fracture gap (1 to 5 mm) and a fixed Elastic Modulus of 60 MPa.



**Range of IFS:**  **Optimal**  **Acceptable**  **Unacceptable**

**Figure 33:** Logarithmic Strain's *maximum* and *minimum* values for the *Wireless Dynamic Plate* in an *Un-Locked* configuration. Focus on the three main *axial* and *tangential components* in a global coordinates system for an increased fracture gap (1 to 5 mm) and a fixed Elastic Modulus of 60 MPa.



**Range of IFS:**



**Optimal**

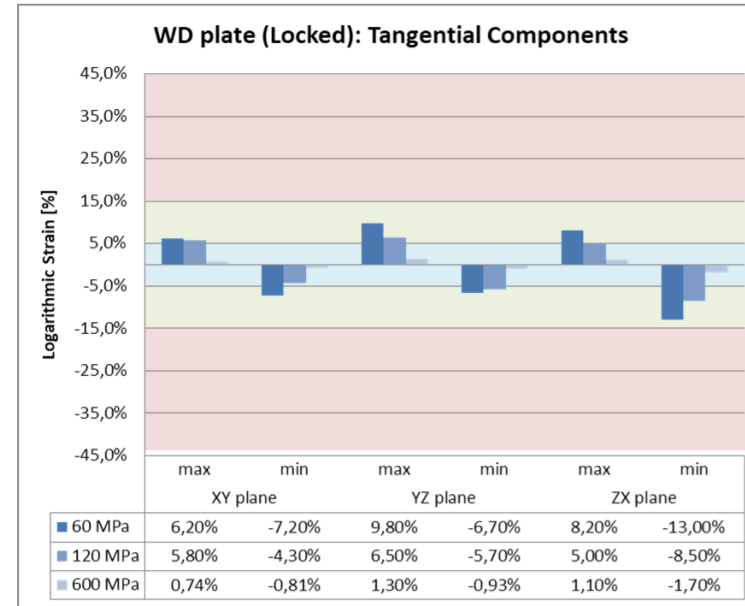
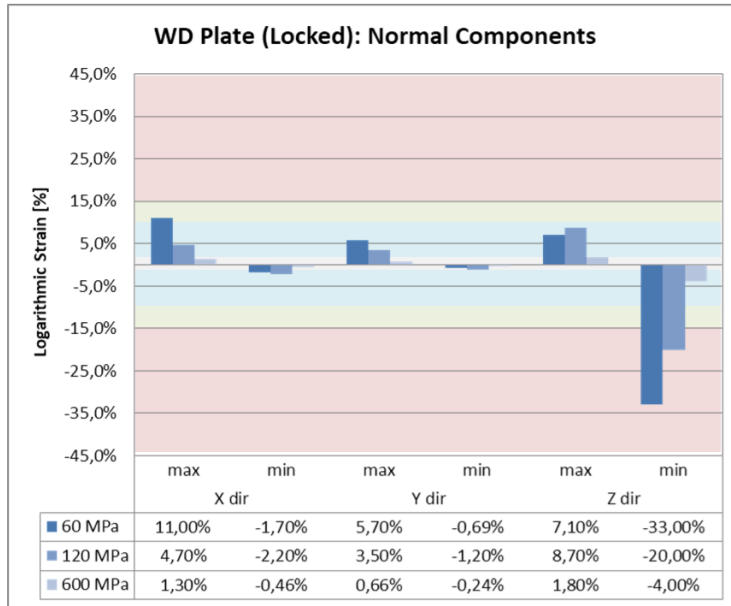


**Acceptable**



**Unacceptable**

**Figure 34:** Logarithmic Strain's *maximum* and *minimum* values for the *Traditional Static Plate*. Focus on the three main *axial* and *tangential* components in a global coordinates system for a fracture gap of 1 mm and an increased callus tissue's Elastic Modulus (from 60 to 600 MPa).



**Range of IFS:**



**Optimal**



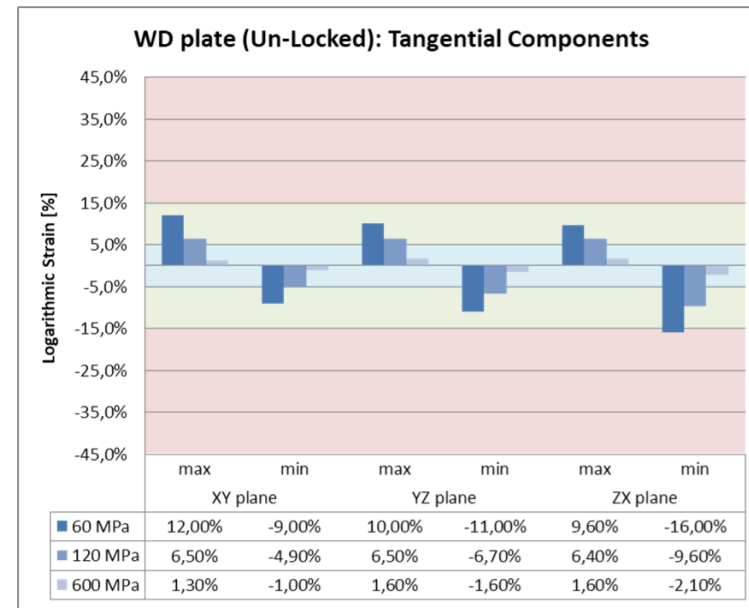
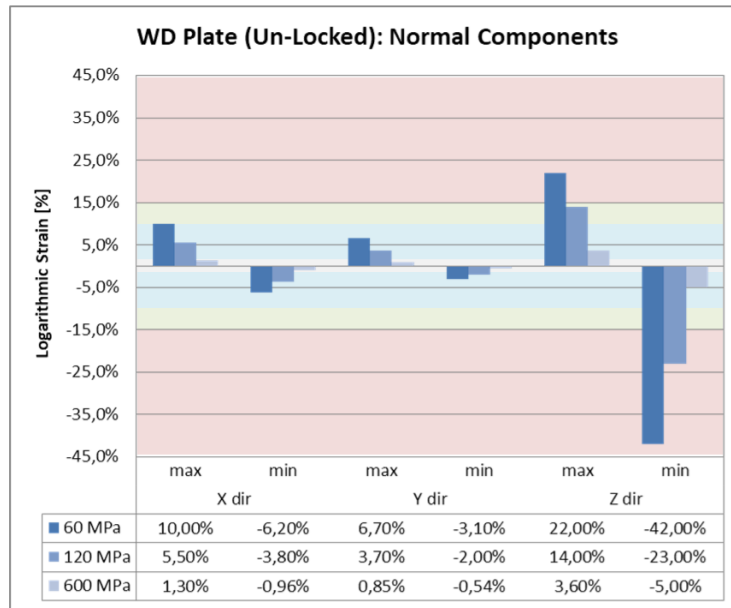
**Acceptable**



**Unacceptable**

**Figure 35:** Logarithmic Strain's *maximum* and *minimum* values for the *Wireless Dynamic Plate* in a *Locked* configuration. Focus on the three main *axial* and *tangential* components in a global coordinates system for a fracture gap of 1 mm and an increased callus tissue's Elastic Modulus (from 60 to 600 MPa).





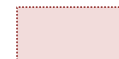
**Range of IFS:**



**Optimal**



**Acceptable**



**Unacceptable**

**Figure 36:** Logarithmic Strain's *maximum* and *minimum* values for the *Wireless Dynamic Plate* in an *Un-Locked* configuration. Focus on the three main *axial* and *tangential* components in a global coordinates system for a fracture gap of 1 mm and an increased callus tissue's Elastic Modulus (from 60 to 600 MPa).

### 5.4.5 Plate structural stiffness without callus tissue

To conclude the analysis, a comparison of the physiologic loading condition, without any callus tissue between the two fracture gaps, has been outlined. In this case, the plate structural stiffness is more significant, and the simulated model would reproduce the first post-operative conditions. The main results have been highlighted in the following figures to highlight both the maximum von Mises stress obtained on the main plate components and the part of the bone that would become in contact with each other. In terms of von Mises stress, results obtained from those analyses can also be feedback to evaluate the accuracy of the existing regulation for plate certification tests.

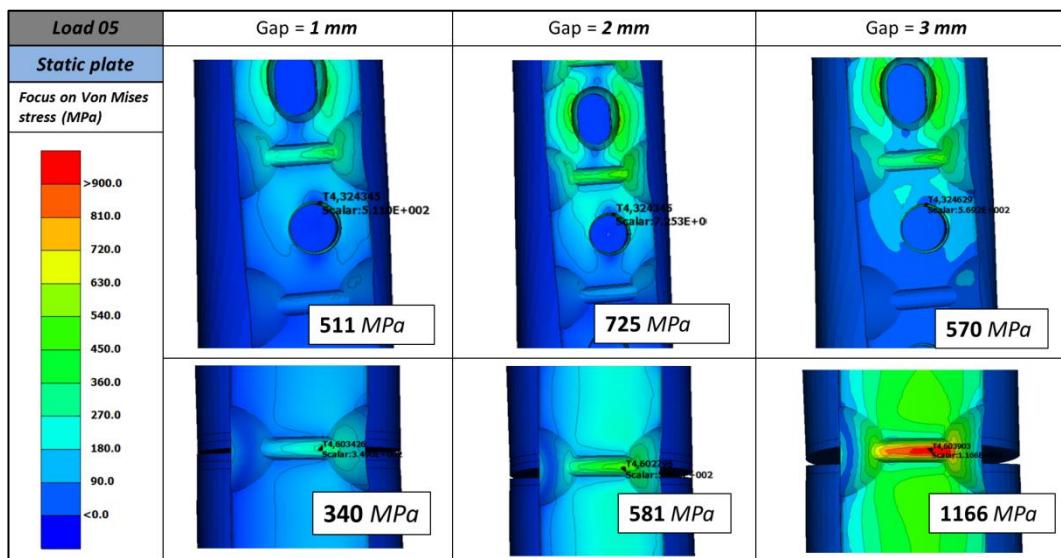


**Figure 37:** Traditional plate *von Mises Stress (MPa)* increases the initial gap. Focus on the main plate body and the most solicited screw hole.

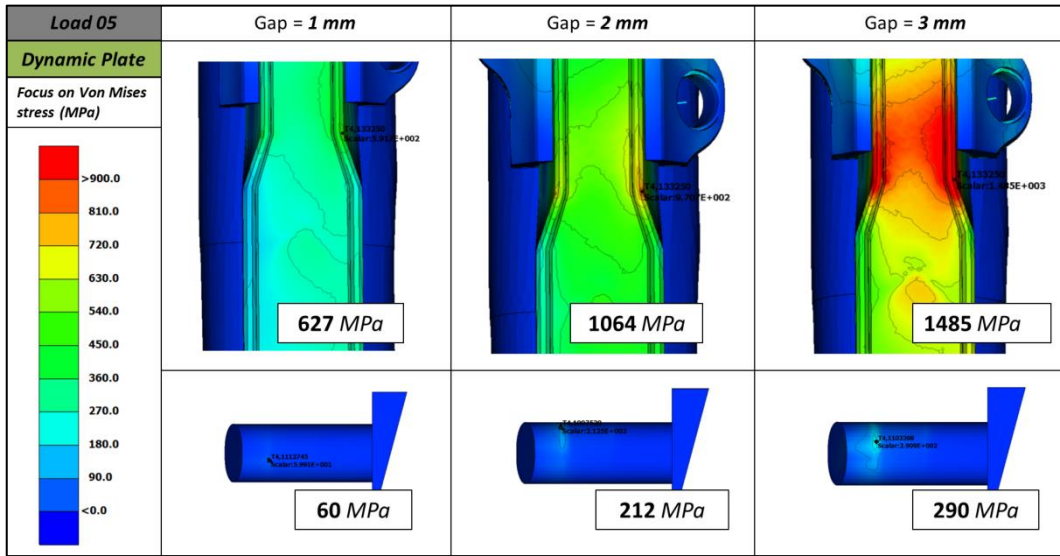


**Figure 38:** Projected dynamic plate von Mises stress (MPa) by increasing the initial gap. Focus on the main plate body and the most pin section.

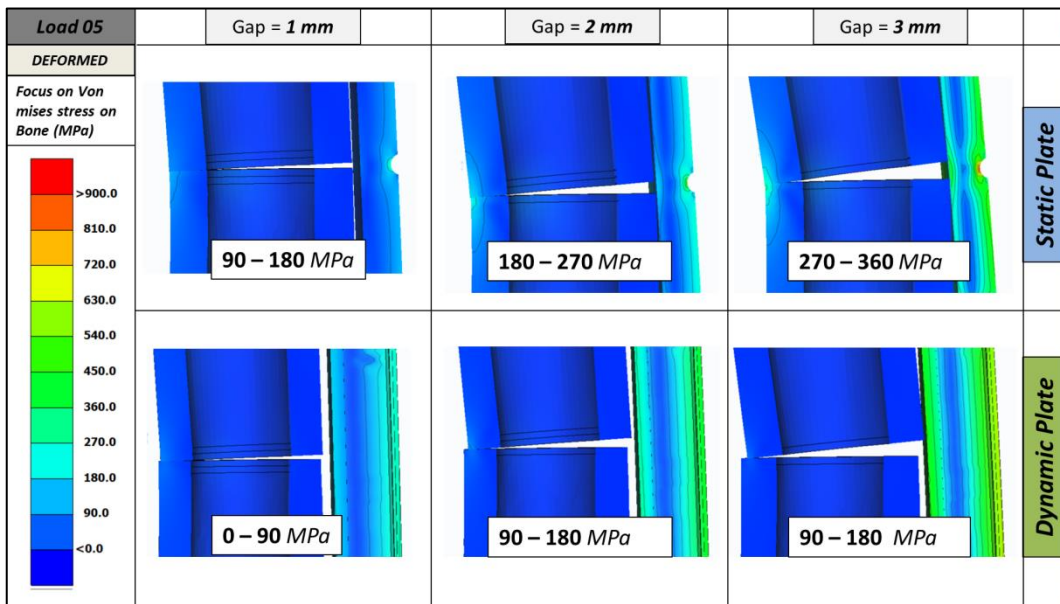


**Figure 39:** Von Mises stress (MPa) on the bone tissue due to initial contact between the two fractured bones. A comparison between the traditional Static Plate and the projected Dynamic Plate in the locked condition has been made.

#### **5.4.6 Main limitations of the analysis**

The main limitation of the analysis is regarding the simulated condition, which referred to the “normal walking” condition, in which it is not possible to check the effect of torsion on the femur load. Another limitation, less critical, could be the type of fracture considered for the analysis, the transversal fracture, which does not represent the entire sample of the clinical fracture. Regarding the modeling and post-processing phases, deformation errors due to callus tissue distortion can represent the first problem, especially for the lower Elastic Modules. The second problem can be the “meshing-border” effect due to the jump from callus tissue to cortical bone, affecting the IFS values. Finally, since the output considered is the Logarithmic Strain, the result strictly depends on the selected Elasticity Modulus.

# Chapter 6

## Conclusion

---

The plate presented is feasible from technical aspects, and its main mechanical and electrical aspects have been deeply investigated. From the results outlined in the previous chapter, the multi-body model gives a brief overview of the maximum power consumption concerning the principal design variable. At the same time, the electromagnetic circuit can be further optimized to give the necessary energy to the conceived transmission system. The plate is structurally safe for all the designed components from a numerical and experimental perspective — the final assembly full-fits both the regulation for commercial purposes and the leading standard of the manufacturing process. The worst stressed point is positioned on the plate body, and the internal interactions have been evaluated using the most accurate tolerances of the physical assembly. The calculated safety factor is about  $1.71$  for the fatigue test with  $R = 0.1$  factor, acceptable for ASTM F382.17 regulation. The flexural stiffness of the bone-plate

system has resulted equal to  $370\text{ N/mm}$ , and a maximum bending moment of  $75.3\text{ kN}\cdot\text{mm}$  can be withstood without plate failure. The numerical results have also highlighted the different behavior for callus stimulation between the conceived Wireless Dynamic Plate and the Traditional Static Plate regarding the physiologic load condition. In particular, the Dynamic Plate offers a symmetrical stimulation of the callus, with less critical negative values in the first post-operative phase. The same plate offers suitable tissue stimulation in significant fractured gaps, while the Traditional Static Plate loses clinical efficacy.

# References

- ASTM International. (2008). *Standard Specification and Test Method for Metallic Bone Plates F382-99*. 1–12. <https://doi.org/10.1520/F0382-17>. Copyright
- Augat, P., Margevicius, K., Simon, J., Wolf, S., Suger, G., & Claes, L. (1998). Local tissue properties in bone healing: Influence of size and stability of the osteotomy gap. *Journal of Orthopaedic Research*, *16*(4), 475–481. <https://doi.org/10.1002/jor.1100160413>
- Barcik, J., Ernst, M., Dlaska, C. E., Drenchev, L., Zeiter, S., Epari, D. R., & Windolf, M. (2021). Programable active fixator system for systematic in vivo investigation of bone healing processes. *Sensors (Switzerland)*, *21*(1), 1–14. <https://doi.org/10.3390/s21010017>
- Bergmann, G., Bergmann, G., Deuretzbacher, G., Deuretzbacher, G., Heller, M., Heller, M., Graichen, F., Graichen, F., Rohlmann, A., Rohlmann, A., Strauss, J., Strauss, J., Duda, G. N., & Duda, G. N. (2001). Hip forces and gait patterns from routine activities. *Journal of Biomechanics*, *34*, 859–871.
- Bishop, N. E., Schneider, E., & Ito, K. (2003). An experimental two degrees-of-freedom actuated external fixator for in vivo investigation of fracture healing. *Medical Engineering and Physics*, *25*(4), 335–340. [https://doi.org/10.1016/S1350-4533\(02\)00250-3](https://doi.org/10.1016/S1350-4533(02)00250-3)
- Blázquez-Carmona, P., Sanchez-Raya, M., Mora-Macías, J., Gómez-Galán, J. A., Domínguez, J., & Reina-Romo, E. (2020). Real-time wireless platform for in vivo monitoring of bone regeneration. *Sensors (Switzerland)*, *20*(16), 1–23.

- <https://doi.org/10.3390/s20164591>
- Bottlang, M., Tsai, S., Bliven, E. K., Von Rechenberg, B., Klein, K., Augat, P., Henschel, J., Fitzpatrick, D. C., & Madey, S. M. (2016). Dynamic stabilization with active locking plates delivers faster, stronger, and more symmetric fracture-healing. *Journal of Bone and Joint Surgery - American Volume*, 98(6), 466–474. <https://doi.org/10.2106/JBJS.O.00705>
- Claes, L. E., & Meyers, N. (2020). The direction of tissue strain affects the neovascularization in the fracture-healing zone. *Medical Hypotheses*, 137, 109537. <https://doi.org/10.1016/j.mehy.2019.109537>
- Claes, L. E., Wilke, H. J., Augat, P., Rübenaeker, S., & Margevicius, K. J. (1995). Effect of dynamization on gap healing of diaphyseal fractures under external fixation. *Clinical Biomechanics*, 10(5), 227–234. [https://doi.org/10.1016/0268-0033\(95\)99799-8](https://doi.org/10.1016/0268-0033(95)99799-8)
- Claes, Lutz E., Heigele, C. A., Neidlinger-Wilke, C., Kaspar, D., Seidl, W., Margevicius, K. J., & Augat, P. (1998). Effects of mechanical factors on the fracture healing process. *Clinical Orthopaedics and Related Research*, 355 SUPPL. <https://doi.org/10.1097/00003086-199810001-00015>
- Clinton T. Rubin and Lance E. Lanyon. (2002). Regulation of Bone Mass by Mechanical Strain Magnitude. *Calcified Tissue International*, 4(10), 803–807. [https://doi.org/10.1002/1527-2648\(20021014\)4:10<803::AID-ADEM803>3.0.CO;2-D](https://doi.org/10.1002/1527-2648(20021014)4:10<803::AID-ADEM803>3.0.CO;2-D)
- Cordey, J., Perren, S. M., & Steinemann, S. G. (2001). Stress protection due to plates: Myth or reality? A parametric analysis made using the composite beam theory. *Injury*, 32. [https://doi.org/10.1016/S0020-1383\(00\)80026-1](https://doi.org/10.1016/S0020-1383(00)80026-1)



- Duda, G. N., Heller, M., Albinger, J., Schulz, O., Schneider, E., & Claes, L. (1998). Influence of muscle forces on femoral strain distribution. *Journal of Biomechanics*, *31*(9), 841–846. [https://doi.org/10.1016/S0021-9290\(98\)00080-3](https://doi.org/10.1016/S0021-9290(98)00080-3)
- E. F. Rybicki, F. A. Simonen and E. B. Weis, J. (1972). ON THE MATHEMATICAL ANALYSIS OF STRESS IN THE HUMAN FEMUR. *Z.a.M.M.*, *52*(10 (OCTOBER, 1972)), 364–371.
- Einhorn, T. A., & Gerstenfeld, L. C. (2015). Fracture healing: mechanisms and interventions. *Nature Reviews Rheumatology*, *11*(1), 45–54. <https://doi.org/10.1038/nrrheum.2014.164>
- Eschweiler, J., Fieten, L., Dell’Anna, J., Kabir, K., Gravius, S., Tingart, M., & Radermacher, K. (2012). Application and evaluation of biomechanical models and scores for the planning of total hip arthroplasty. *Proceedings of the Institution of Mechanical Engineers, Part H: Journal of Engineering in Medicine*, *226*(12), 955–967. <https://doi.org/10.1177/0954411912445261>
- Fadhel, Y. Ben, Ktata, S., Sedraoui, K., Rahmani, S., & Al-Haddad, K. (2019). A modified wireless power transfer system for medical implants. *Energies*, *12*(10). <https://doi.org/10.3390/en12101890>
- Foxworthy, M., & Pringle, R. M. (1995). Dynamization timing and its effect on bone healing when using the Orthofix Dynamic Axial Fixator. *Injury*, *26*(2), 117–119. [https://doi.org/10.1016/0020-1383\(95\)92189-H](https://doi.org/10.1016/0020-1383(95)92189-H)
- Gautier, E., Perren, S. M., Cordey, J., Steinemann, S. G., Borgeaud, M., & Leyvraz, P. F. (2001). Effect of plate position relative to bending direction on the rigidity of a plate osteosynthesis. A theoretical analysis. *Injury*, *32*(SUPPL. 3), 14-20+78. [https://doi.org/10.1016/S0020-1383\(01\)00057-2](https://doi.org/10.1016/S0020-1383(01)00057-2)

- Ghiassi, M. S., Chen, J., Vaziri, A., Rodriguez, E. K., & Nazarian, A. (2017). Bone fracture healing in mechanobiological modeling: A review of principles and methods. *Bone Reports*, 6, 87–100. <https://doi.org/10.1016/j.bonr.2017.03.002>
- Giannoudisa, P. V., & \*, Thomas A. Einhornb, D. M. (2011). Fracture healing: The diamond concept. *American Journal of Physical Anthropology*, 144(4), 287.
- Glatt, V., Evans, C. H., & Tetsworth, K. (2017). A concert between biology and biomechanics: The influence of the mechanical environment on bone healing. *Frontiers in Physiology*, 7(JAN), 1–18. <https://doi.org/10.3389/fphys.2016.00678>
- Goodship, A. E., Lawes, T. J., & Rubin, C. T. (2009). Low-magnitude high-frequency mechanical signals accelerate and augment endochondral bone repair: Preliminary evidence of efficacy. *Journal of Orthopaedic Research*, 27(7), 922–930. <https://doi.org/10.1002/jor.20824>
- Gulati, D., Aggarwal, A. N., Kumar, S., & Agarwal, A. (2012). Skeletal injuries following unintentional fall from height. *Ulusal Travma ve Acil Cerrahi Dergisi*, 18(2), 141–146. <https://doi.org/10.5505/tjtes.2012.12058>
- Gutekunst & Co. (n.d.). *No Title*.
- Hannouche, D., Petite, H., & Sedel, L. (2001). Current trends in the enhancement of fracture healing. *Journal of Bone and Joint Surgery - Series B*, 83(2), 157–164. <https://doi.org/10.1302/0301-620X.83B2.12106>
- Heller, M. O., Bergmann, G., Kassi, J. P., Claes, L., Haas, N. P., & Duda, G. N. (2005). Determination of muscle loading at the hip joint for use in pre-clinical testing. *Journal of Biomechanics*, 38(5), 1155–1163. <https://doi.org/10.1016/j.jbiomech.2004.05.022>
- Henschel, J., Tsai, S., Fitzpatrick, D. C., Marsh, J. L., Madey, S. M., & Bottlang, M.

- (2017). Comparison of 4 Methods for Dynamization of Locking Plates: Differences in the Amount and Type of Fracture Motion. *Journal of Orthopaedic Trauma*, 31(10), 531–537. <https://doi.org/10.1097/BOT.0000000000000879>
- Hente, R., & S.M., P. (2018). Mechanical Stimulation of Fracture Healing – Mechanická stimulace hojení zlomenin – stimulace svalku prodloužením fáze. *Acta Chir Orthop Traumatol*, 6, 385–391.
- Larsson, S., Kim, W., Caja, V. L., Egger, E. L., Inoue, N., & Chao, E. Y. S. (2001). Effect of early axial dynamization on tibial bone healing: A study in dogs. *Clinical Orthopaedics and Related Research*, 388, 240–251. <https://doi.org/10.1097/00003086-200107000-00033>
- Lee, T. C. (1999). Bone remodeling: Should we cry, Wolff? *Irish Journal of Medical Science*, 168(2), 102–105. <https://doi.org/10.1007/bf02946474>
- Morlock, M., Schneider, E., Bluhm, A., Vollmer, M., Bergmann, G., Müller, V., & Honl, M. (2001). Duration and frequency of everyday activities in total hip patients. *Journal of Biomechanics*, 34(7), 873–881. [https://doi.org/10.1016/S0021-9290\(01\)00035-5](https://doi.org/10.1016/S0021-9290(01)00035-5)
- Otte, D.\*; Haasper, C. \*\*. (2017). CHARACTERISTICS ON FRACTURES OF TIBIA AND FIBULA IN CAR IMPACTS TO PEDESTRIANS AND BICYCLISTS – INFLUENCES OF CAR BUMPER HEIGHT AND SHAPE. *51st ANNUAL PROCEEDINGS ASSOCIATION FOR THE ADVANCEMENT OF AUTOMOTIVE MEDICINE*. [http://digilib.unila.ac.id/4949/15/BAB II.pdf](http://digilib.unila.ac.id/4949/15/BAB%20II.pdf)
- Perren, S. M. (2002). Evolution of the internal fixation of long bone fractures: The scientific basis of biological internal fixation: choosing a new balance between stability and biology. *The Journal of Bone and Joint Surgery*, 84(8), 1093–1110.

<https://doi.org/10.1302/0301-620X.84B8.13752>

Robert C. Juvinall, K. M. M. (2012). *Fundamentals of Machine Component Design*. (John Wiley & Sons (ed.); fifth edit).

SA., L. K. (n.d.). *AISI 316 LVM Implant: Materials and Raw Manufacturing Data*. Retrieved August 10, 2020, from [www.kleinmetals.ch/steel/316-lvm-f-138-implants.htm](http://www.kleinmetals.ch/steel/316-lvm-f-138-implants.htm)

Salisbury Palomares, K. T., Gleason, R. E., Mason, Z. D., Cullinane, D. M., Einhorn, T. A., Gerstenfeld, L. C., & Morgan, E. F. (2009). Mechanical stimulation alters tissue differentiation and molecular expression during bone healing. *Journal of Orthopaedic Research*, 27(9), 1123–1132. <https://doi.org/10.1002/jor.20863>

Sonderegger, J., Grob, K. R., & Kuster, M. S. (2010). Dynamic plate osteosynthesis for fracture stabilization: how to do it. *Orthopedic Reviews*, 2(1), 4. <https://doi.org/10.4081/or.2010.e4>

Steiner, M., Claes, L., Ignatius, A., Niemeyer, F., Simon, U., & Wehner, T. (2013). Prediction of fracture healing under axial loading, shear loading and bending is possible using distortional and dilatational strains as determining mechanical stimuli. *Journal of the Royal Society Interface*, 10(86). <https://doi.org/10.1098/rsif.2013.0389>

Steiner, M., Claes, L., Ignatius, A., Simon, U., & Wehner, T. (2014a). Disadvantages of interfragmentary shear on fracture healing - Mechanical insights through numerical simulation. *Journal of Orthopaedic Research*, 32(7), 865–872. <https://doi.org/10.1002/jor.22617>

Steiner, M., Claes, L., Ignatius, A., Simon, U., & Wehner, T. (2014b). Numerical simulation of callus healing for optimization of fracture fixation stiffness. *PLoS*

ONE, 9(7), 1–11. <https://doi.org/10.1371/journal.pone.0101370>

Steiner, M., Claes, L., Ignatius, A., Simon, U., & Wehner, T. (2014c). Disadvantages of interfragmentary shear on fracture healing-mechanical insights through numerical simulation. *Journal of Orthopaedic Research*, 32(7), 865–872. <https://doi.org/10.1002/jor.22617>

Taljanovic, M. S., Jones, M. D., Ruth, J. T., Benjamin, J. B., Sheppard, J. E., & Hunter, T. B. (2003). Fracture Fixation. *Radiographics*, 23(6), 1569–1590. <https://doi.org/10.1148/rg.236035159>

Terzini, M.; Serino, G.; Lugas, T.A.; Dichio, G.; Costa, P.; Audenino, A.L. Strategies to Speed up the Standardized Bone Plates Mechanical Testing for Regulatory Purposes; Pedrizetti, G., Accardo, A., Marceglia, S., Brun, F., Eds.; 2020; Available online: <https://portal.issn.org/resource/ISSN/2724-2129>

Tufekci, P., Tavakoli, A., Dlaska, C., Neumann, M., Shanker, M., Saifzadeh, S., Steck, R., Schuetz, M., & Epari, D. (2018). Early mechanical stimulation only permits timely bone healing in sheep. *Journal of Orthopaedic Research*, 36(6), 1790–1796. <https://doi.org/10.1002/jor.23812>

Wolff, J., & Wolff, J. (1986). The Internal Architecture of Normal Bone and Its Mathematical Significance. *The Law of Bone Remodelling*, 1832, 3–22. [https://doi.org/10.1007/978-3-642-71031-5\\_2](https://doi.org/10.1007/978-3-642-71031-5_2)

Yamaji T, Ando K, Wolf S, Augat P, & Claes L. (2001). The effect of micromovement on callus formation. *Journal of Orthopaedic Science*, 6(6), 571–575.

Yaneva-Deliverska, M., Deliversky, J., & Lyapina, M. (2015). BIOCOMPATIBILITY OF MEDICAL DEVICES – LEGAL REGULATIONS IN THE EUROPEAN UNION. *Journal of IMAB - Annual Proceeding (Scientific Papers)*, 21(1), 705–708.

<https://doi.org/10.5272/jimab.2015211.705>

Zyga, S. (2011). Application of ISO 13485:2003 in Biomedical Engineering: a Systematic Review. *International Journal of Caring Sciences*, 4(2), 58–65.